Facies association analysis of a Toarcian siliciclastic-carbonate lacustrine system, Sichuan Basin, China

Hang Cui [a,b], Shifa Zhu [a,b,*], Chao Liang [c], Weize Ma [a,b], Huan Tong [a,b], Zhensheng Shi [d]

[a] National Key Laboratory of Petroleum Resources and Engineering, China University of Petroleum (Beijing), Beijing 102249, China
[b] College of Geosciences, China University of Petroleum, Beijing 102249, China
[c] College of Geosciences, China University of Petroleum (East China), Qingdao 266580, China
[d] PetroChina Research Institute of Petroleum Exploration and Development, Beijing 100083, China

ARTICLE INFO

ABSTRACT

Globally, considerable coverage has been devoted to marine environment affected by the Jenkyns Event, but little attention has been given to lacustrine system. Here, siliciclastic-carbonate samples of the Da'anzhai Member (J$_1$dn) were examined for petrology and geochemistry in order to evaluate lithofacies characteristics, depositional processes and environmental changes of the palaeo-Sichuan lacustrine basin contemporaneous with the Jenkyns Event. Unique sedimentological and petrological features were used to identify five principal facies associations (FA) and depositional environments, including the distal delta front, accretionary bioclastic shoals, proximal bioclastic shoal ramp, distal bioclastic shoal ramp and (semi-)deep lacustrine environment. The vertical transitions of FA reveal that J$_1$dn forms a complete lacustrine transgressive-regressive sedimentary system during the Toarcian, which can be further divided into 3 units in combination with standard gamma logging. The lower unit is characterised by frequent intermixing of multiple FA interpreted as frequent lake-level fluctuations. The middle unit is characterised by the deposition of clay-rich mudstone and the demise of bioclastic shoals interpreted as intensive lacustrine transgression that were at times affected by storm-induced waves or oscillatory currents coinciding with the initiation of the Jenkyns Event. The upper unit is characterised by the thicker and higher proportion of biogenic carbonate-rich lithofacies interpreted as the lake regression, contemporaneous with the end of the Jenkyns Event. Overall, clay-rich lithofacies from suspension settling, turbidity current or slumping triggered by storm events were deposited during a high relative lacustrine-level, accompanied by organic carbon-rich deposition and preservation. In contrast, carbonate-rich lithofacies were mainly controlled by biogenic carbonate sedimentation, associated with a low relative lacustrine-level unconducive to organic matter accumulation. Finally, the proposed depositional evolution model at the lake-level highstand stage and lowstand stage of the palaeo-Sichuan lacustrine basin provides new insights and understanding on the changing palaeolimnological history of the Toarcian lacustrine system.

1. Introduction

The Jenkyns Event has been confirmed as a transient period of environmental perturbations during the Toarcian Stage, Mesozoic Era (Hesselbo et al., 2007; Jenkyns, 2010; Krencker et al., 2019). Associated with the rapid formation and transport of greenhouse gases into the atmosphere (Svensen et al., 2007; Dera et al., 2009), the Jenkyns Event has been estimated to commence at ~183 Ma (Pálfy and Smith, 2000; Pieńkowski et al., 2016) and lasted for about 300,000–500,000 years (Boulila et al., 2014; Sell et al., 2014). The universally accepted triggering mechanism for the Jenkyns Event is the release of thermogenic

methane and CO$_2$ due to Karoo-Ferrar Large Igneous Province magmatism in the Southern Hemisphere and biogenic methane from dissociation of the sub-seafloor (Duncan et al., 1997; Pálfy and Smith, 2000; McElwain et al., 2005; Svensen et al., 2007; Xu et al., 2017; Remírez and Algeo, 2020). The resulting climatic, hydrologic and biological feedbacks of the marine environment have been extensively documented by petrological and geochemical characteristics from marine sedimentary rocks, including considerable impact in sea level rises and the subsequent rapid transgression (e.g. Ahokas et al., 2014; Pittet et al., 2014), elevated seawater temperatures (e.g. Bailey et al., 2003; Ruebsam et al., 2020), major extinction of marine organisms (e.g. Harries and Little,

1999; Danise et al., 2015), and enhanced primary productivity (e.g. Ullmann et al., 2014; Ruebsam et al., 2018; Xu et al., 2018). However, considerable coverage has been devoted to hydrologic and biological feedbacks and carbon sequestration in marine environments, with scant attention paid to lacustrine system during the Jenkyns Event (e.g. Ordos Basin, Jin et al., 2020; Jinyang Basin, Liu et al., 2020b).

Climatic, hydrologic and biological information during the Jenkyns Event in the Early Jurassic Period has also been extensively recorded by the mixed siliciclastic-carbonate sediments in the Da'anzhai Member (J_1dn) of the palaeo-Sichuan lacustrine basin, providing a 'natural laboratory' for researching the petrological characteristics and its implications for historical palaeolimnological change. Some scholars, having confirmed the connection between J_1dn and the Jenkyns Event, first pinpointed that the *Re-Os* radioisotopic dating of J_1dn samples provides a well-constrained single isochron of 180 ± 3.2 Ma, which coincided with the timing of the Jenkyns Event (Xu et al., 2017). Subsequently, Liu et al. (2020a, 2022) further studied the hydrological conditions of the Toarcian Sichuan lacustrine basin, pointing out that the lake water column experienced frequent anoxic-ferruginous conditions interspersed with significant euxinic episodes, and revealed that the relative

water-level fluctuations were consistent with contemporaneous global sea levels. However, although these few studies tended to pay too much attention to the application of geochemical proxies, they lacked detailed descriptions and interpretations on the petrological characteristics. Overall, the J_1dn succession is characterised by thick, mixed siliciclastic-carbonate deposits (ca 100 m thick). These deposits display great diversity in lithofacies and thickness, and are unlike typical carbonate parasequences, giving rise to the following questions: How are the lithofacies in the J_1dn succession divided and what are the depositional processes of each lithofacies? What is the vertical variation of different types of lithofacies? Can a link between lithofacies changes and the Jenkyns Event be established?

Therefore, we have undertaken an investigation of J_1dn mainly from a petrological perspective (hand-sample observations and multiple micro-analytical techniques), and supplemented extant studies with new geochemical analyses and validations. The specific goals of this article are to: (1) define the lithofacies and facies associations of the J_1dn mixed sediments and interpret the depositional processes; (2) describe the observed vertical lithofacies variability; and (3) evaluate the lacustrine depositional environment and propose the mixed carbonate-siliciclastic
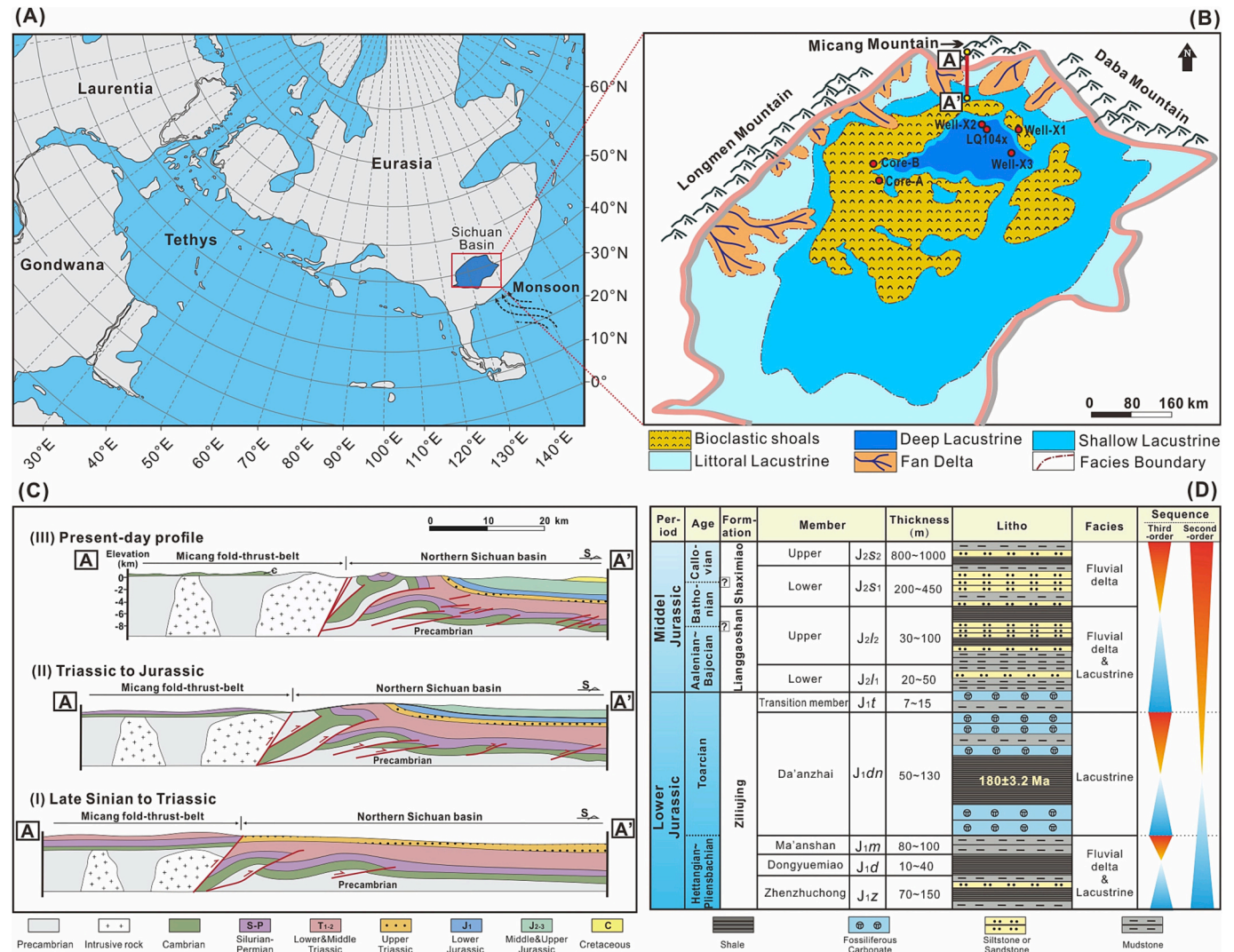

Fig. 1. (A) The location of the palaeo-Sichuan lacustrine basin at 179 Ma (modified form Xu et al., 2017). This map shows a regional tectonic plate reconstruction. (B) Well location and detailed palaeogeography of J_1dn within the Sichuan Basin (modified form Feng et al., 2015). The red circles represent the well locations. (C) Typical cross section across the north segment of the Longmen fold-thrust belt and its evolution profiles (Luo et al., 2015). The location of the cross section is shown in Fig. 1B. (D) Simplified stratigraphic column for the Lower Jurassic in the Sichuan Basin. The Da'anzhai Member (study interval) exhibits alternating beds of fossiliferous carbonate rock and clay-rich mudstone. Radioisotopic dating of the Da'anzhai samples provides the results of ~183 Ma, which can be confirmed to be of the Toarcian age (Xu et al., 2017). (For interpretation of the references to colour in this figure legend, the reader is referred to the web version of this article.)

depositional model of Sichuan Basin during the Toarcian.

2. Geological settings

The Sichuan Basin is a typical multi-cycle superposed petroliferous basin in China, covering a total area of ca. 230,000 km^2 (Cai et al., 2003). During the Early Jurassic, the palaeo-Sichuan Basin was located in the mid-latitudes, surrounded by mountains towards northwest and adjoining oceans towards the southeast (Liu et al., 2022; Fig. 1A). Three wells covered in this study, Well X1 to Well X3, were taken from the north-central part of the basin (Fig. 1 B).

The basin is dominated by three stages of basin evolution: (1) a marine carbonate platform from the Late Sinian to Middle Triassic, (2) a foreland basin from the Late Triassic to Late Cretaceous, and (3) subsequent structural modification (Fig. 1C) (Liu et al., 2021). Influenced by the Indo-Sinian movements during the Late Permian to Late Triassic, the palaeo-uplift resulted in the transition from marine environments to terrestrial deposition of the basin (Liu et al., 2021). The basin mainly developed into an inland freshwater lacustrine-fluvial delta depositional system during the Early Jurassic. The depositional period of the Da'anzhai member in the Ziliujing Formation was the stage when the internal tectonic action was weak whilst the surrounding orogenic belt activity was stable (Xiao et al., 2021). During this period, the overall subsidence rate of the basin was substantially greater than the accumulation rate of terrigenous detritus, resulting in the formation of the largest lacustrine basin in the Early Jurassic, that established good conditions for the enrichment of organic-rich sediments.

The basin's floor exposes around the Yangtze platform, and the sedimentary cover is composed of Palaeozoic and Middle Mesozoic shallow marine deposits and younger terrestrial strata (Liu et al., 2021). The Early-Middle Jurassic system in Sichuan Basin is dominated by clastic rocks and limestone, including the Ziliujing Formation, Lianggaoshan Formation and Shaximiao Formation. The Ziliujing Formation can be further divided into Zhenzhuchong Member (J_1z), Dongyuemiao Member (J_1d), Ma'anshan Member (J_1m), Da'anzhai Member (J_1dn, the study strata) and Transition Member (J_1t) from below (Fig. 1D). J_1dn exhibits the mixing of widespread sedimentation of fossiliferous carbonate rock and massive or laminated clay-rich mudstone, occurring continuously throughout the lacustrine basin (Li et al., 2013; Feng et al., 2015; Chen et al., 2015; Xiao et al., 2021).

Significant negative carbon-isotope excursion (CIE) in organic-rich sediments, carbonates, fossil wood and various organic biomarkers has been observed during the Jenkyns Event (e.g., Schouten et al., 2000; Hermoso et al., 2009), which was most developed on the Northwest and Southwest European Shelf (Cohen et al., 2004; Hesselbo et al., 2007; Hermoso et al., 2012; Kafousia et al., 2014; Suan et al., 2018). In the above-mentioned areas, the CIE value of organic carbon can reach −5 to −10‰ (Appendix A). However, a growing number of studies suggest that the CIE during the Jenkyns Event is not only a European phenomenon, but a global one (e.g., Them et al., 2017; Xu et al., 2017). Therefore it can serve as a marker for chemostratigraphic and chronostratigraphic indicators. Further, recent studies have revealed the existence of CIE in the organic-rich sediments of J_1dn of the palaeo-Sichuan lacustrine basin. For example, CIE has been observed in two wells (X2 and LQ104, Appendix A) by Liu et al. (2020a), and another two cores (Core-A and Core-B, Appendix A) by Xu et al. (2017) (Fig. 1B for the well location). Therefore, combined with the *Re-Os* radioisotopic dating of Middle J_1dn shale samples (180 ± 3.2 Ma, Xu et al., 2017), this is sufficient to demonstrate that the depositional period of J_1dn corresponds well with the Jenkyns Event.

3. Samples and methods

A total of 3 typical drilling cores in the palaeo-Sichuan Basin were examined in this study (see Fig. 1B for the location). Depositional processes and environment identified in the cores were recorded in detail, including lithology, grain-size variations, lamination style, sedimentary structures, fossil type and abundance, colour, and any other outstanding features. Subsequently, samples were collected from these 3 wells for systematic petrographic and geochemical characterisation (refer to Appendix B for all sample information). Commonly, the physical and biologic characteristics preserved in mudstones cannot be interpreted only from a macroscopic perspective (Lazar et al., 2015). Thus, the interpretation of depositional processes and environment also integrates multiple micro-analytical techniques.

3.1. Petrography

Thin sections of 60 samples from Well X1 were made to observe both the microfacies framework and the proportion, size and frequency of fossil fragments. All thin sections were stained with alizarin red-S solution to facilitate recognition of carbonate minerals. Photomicrographs were captured by metallographic microscope BX51 produced by Olympus, utilising a 12 V/100 W halogen lamp as the light source. The optical acquisition system is Olympus Stream provided by Olympus Soft Imaging Solutions GmbH. Images were photographed at a resolution of 4800 × 3600 pixels, and stored as a JPG file.

A total of 10 samples from Well X1 were selected for surface and morphology observation. Of these, 6 freshly broken rock samples coated with a gold film on the surface and 4 argon-ion milled samples were integrated to image using scanning electron microscopy (GeminiSEM 300, Carl Zeiss, Germany). All SEM photographs of freshly broken rock samples were taken at an accelerating voltage of 10 kV, and all argon-ion milled samples at 8 kV. The magnification ranged from ×12 to ×2,000,000. Images were photographed under the same conditions at a resolution of 1024 × 768 pixels and stored as a TIFF file.

To understand the mineralogy, 27 rock samples from Well X1 were milled to fine powder (<2 μm) using a mortar and pestle. Powdered samples were then dried in an oven for X-ray diffraction analysis. Bulk-rock analysis was performed following the method used by Šegvić et al. (2016). Subsequently, clay fraction separation was carried out by centrifugation for 16 clay-rich mudstone samples from Well X1. Oriented clay sections of these fractions were prepared for the semiqualitative measurements of clays. The analysis of both bulk rock and clay fractions was carried out using a Rigaku D/MAX-2600PC X-ray diffractometer with Cu-Kα radiation, from $2θ = 5°$ up to 65° at a scanning rate of 2°/min. The generator settings were 40 kV and 25 mA, with a temperature of 25 °C and a humidity of 40%.

3.2. Geochemistry

A total of 88 powdered rock samples were analysed by the Rock-Eval 6 Standard Analyzer unit (Vinci Technologies, Nanterre, France) for programmed pyrolysis. Pyrolysis samples from Well X1 and Well X3 were selected with no strictly equal intervals, but each sampling point is as close to synchronous sampling point as possible. An aliquot of 45–80 mg samples was weighed into crucibles and inserted into the device. The temperature profile is 300–650 °C and 300–850 °C for the pyrolysis and oxidation ovens, respectively. The total organic carbon (TOC, %), S1, S2, Tmax, and S4 were determined and used to calculate the hydrogen index (HI).

Additionally, the bulk concentrations of TOC were analysed in 11 sidewall core samples in Well X3. All of the sidewall core samples were crushed and ground to a diameter of <0.2 mm. Then, dilute hydrochloric acid (1.5 mol/L) was added to each sample to remove the carbonates. The acidification process was repeated at least three times until no reaction was observed. Finally, all of the samples were washed with deionised water and put into the oven to dry. Samples were analysed using a LECO CS230 carbon analyzer.

4. Lithofacies and facies association characterisation

Through the documentation of colour, sedimentary structure, grain size characteristics and trace-fossil diversity, 12 lithofacies (LF) were recognised according to hand-sample observations and multiple microanalytical techniques (Fig. 2). These lithofacies were subsequently identified and delineated into five principal facies associations (FA) in J$_1$dn, combining lithofacies of similar depositional environment. Here, taking Well X1 as an example, these FA are described in detail.

4.1. FA1

Laminated siltstone occurred throughout this FA, which are unique in terms of outlined recognition criteria. FA1 contains a variety of different sedimentary structures but is volumetrically dominant by frequently interbedded siltstones and mudstones with individual lamination and a thickness of <1.0 cm (LF2). Based on colour variation, the lighter grey laminae are identified as siltstones and the darker grey as mudstones. Sedimentary structure in siltstone laminae principally includes subhorizontal parallel lamination and unidirectional low-angle cross lamination (Fig. 3A-3C). Siltstone laminae commonly display

minor basal scours disposed over a sharp boundary or loading features into softer mudstone laminae below. Inside the mudstone laminae, millimetre to several centimetre-scale mottled texture and subjacent burrows can be moderately observed (LF3; Fig. 3A, C), exhibiting a suite of diminutive bioturbation. Interlaminated siltstones cross-cut heterolithic mudstone regions vertically and laterally, resulting discontinuous mudstone intervals across the core. By contrast, the proportion of pure siltstones with low-angle wedge cross-stratification as well as planar lamination (LF1) is low but do exist (Fig. 3B). In thin sections, the silt particles are composed primarily of subrounded monocrystal quartz as well as containing minor content of feldspar, mica flakes, rip-up plant clasts, which present well subparallel alignments (Fig. 3D-3G). The interstitial materials are mainly composed of detrital clay minerals with minor carbonate cements.

4.2. FA2

The hand samples of this FA are predominantly light grey or yellowish-brown in colour, comprised principally of a diverse suite of calcified bioclasts disseminated in carbonate cements. In terms of sedimentary structure, FA2 can be subdivided into two distinct lithofacies:
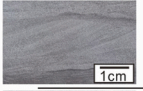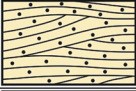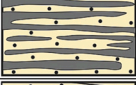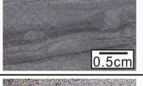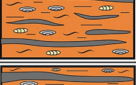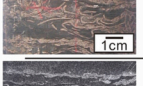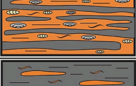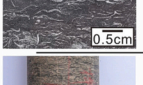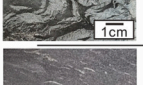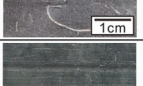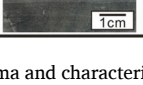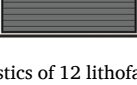
Type	Lithology	Photos	Sketch	Main distribution	Descriptions	Interpretations
L1	Siltstone			FA1	Siltstone with low-angle wedge cross stratification or planar lamination.	Unidirectional tractional deposition by relative high-concentration flow of delta front
L2				FA1	Siltstone and mudstone are interbedded frequently with individual lamination and a thickness of less than 1.0 cm.	Traction plus fallout processes from flows with high suspended loads of distal delta front
L3				FA1	Mostly interbedded siltstone and mudstone with rhythmites and planar lamination. Mottled texture and distinct burrow from diminutive bioturbation can be observed.	
L4	Fossiliferous carbonate			FA2	Fossiliferous limestone with parallel-to-wavy bedding, primarily consisting of bivalve and ostracod shell fragments in sub-horizontal alignments.	Fast bio-carbonate deposition in tranquil conditions
L5				FA2	Fossiliferous limestone with chaotic bedding, composed of randomly scattered bivalve and ostracod shell fragments.	Fast bio-carbonate deposition probably in-situ remobilised, resuspended and redeposited by storms.
L6	Mixing of fossiliferous carbonate and mudstone			FA3	Fossiliferous limestone with rhythmical and discontinuous mudstone interlaminations occurring between millimetre and multiple centimetre intervals.	Mixed bio-carbonate deposition and suspension settling in tranquil conditions triggered by oscillation of the relative lake level
L7				FA3, FA4	Interbedded fossiliferous limestone and clay-rich mudstone with parallel-to-wavy bedding. The proportions of two components are virtually the same.	
L8				FA4	Clay-rich mudstone with rhythmical and discontinuous fossiliferous limestone interlaminations occurring between millimetre and multiple-centimetre intervals.	
L9				FA3	Mixing of fining-upward and scattered bivalve, ostracod shell fragments and mudstone component.	Mixed bio-carbonate deposition and suspension settling along with storm-induced wave or oscillatory current.
L10				FA3	Interbedded fossiliferous limestone and clay-rich mudstone with contorted bedding, slump structure and deformed lamination.	
L11				FA4	Massive to faintly laminated mudstone containing fine floating bivalve and ostracod shell fragments.	Suspension settling with minor distal diluted gravitational flows.
L12	Mudstone (or shale)			FA5	Massive to laminated mudstone with dark grey or black colour and uniform grain size. Almost no shell fragments can be observed.	Anoxic conditions with suspension settling of sediments in low flow regimes.

Fig. 2. Conceptual schema and characteristics of 12 lithofacies recognised in the study area. Lithofacies were divided mainly by colour, sedimentary structure, grain size characteristics and trace-fossil diversity.
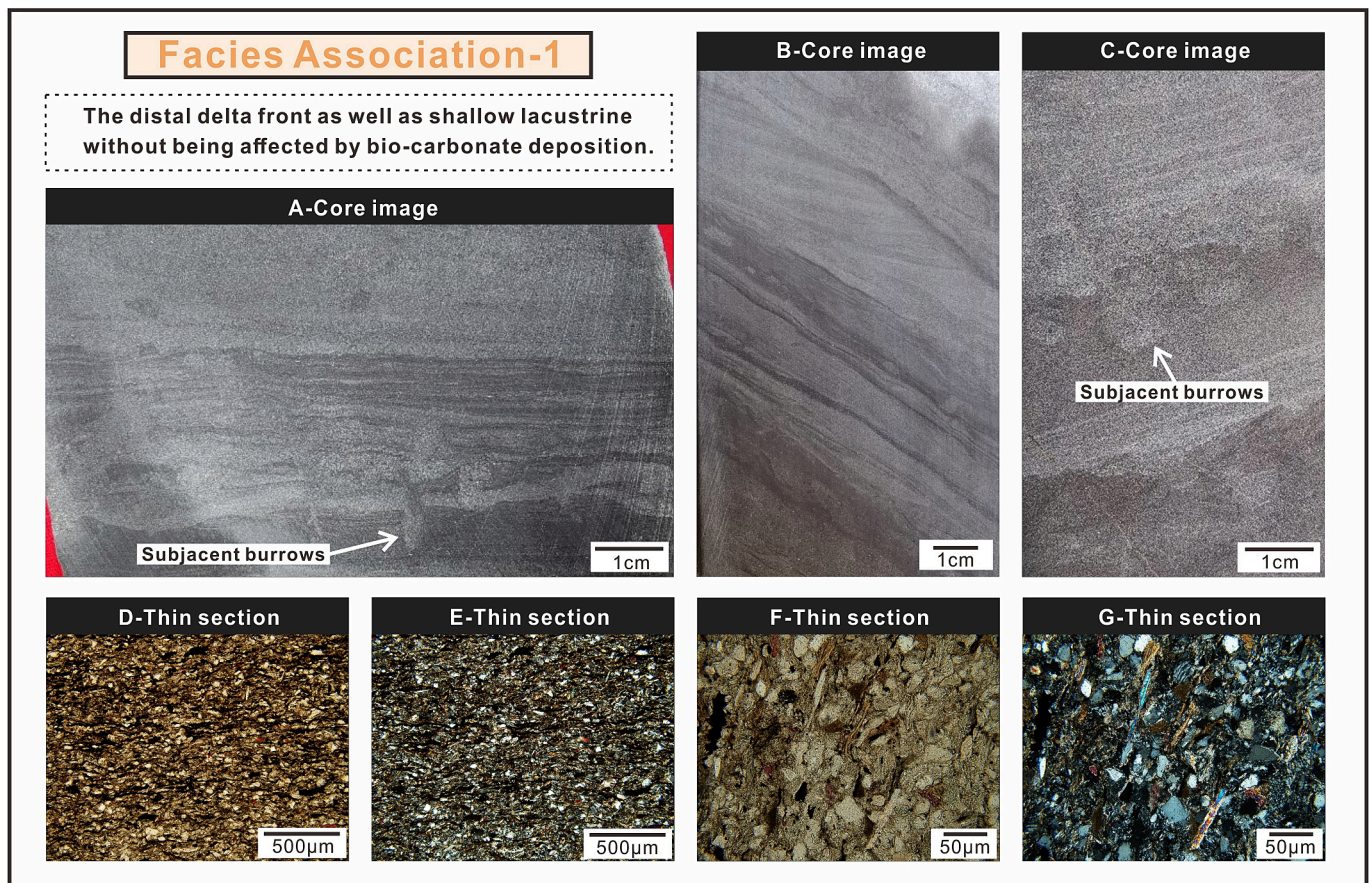
Fig. 3. Overview and examples of key features for FA1. (A) Interbedded siltstone and mudstone with mottled texture and distinct burrow. Well X1, 3161.40 m; (B) Siltstones with low-angle wedge cross-stratification. Well X1, 3161.60 m; (C) Mudstone component with mottled texture and distinct burrow. Well X1, 3207.50 m; (D) Under PPL and (E) under XPL are from the same location within a thin section. The clastic grains are composed of quartz, feldspar, mica flakes and rip-up plant clasts, which present well subparallel alignments. Well X1, 3162.11 m; (F) Under PPL and (G) under XPL are from the same location within a thin section. The mica flakes and rip-up plant clasts present well subparallel alignments. Well X1, 3158.60 m. PPL, plane-polarised light; XPL, cross-polarised light.

LF4–Fossiliferous limestone with parallel-to-wavy bedding, primarily consisting of bioclasts in sub-horizonal alignments (Fig. 4A); and LF5–Fossiliferous limestone with chaotic bedding, composed of randomly scattered bioclasts (Fig. 4B, C). Calcified bioclasts are generally intact in LF4 and intact to broken in LF5. Compositionally, LF4 and LF5 consist predominantly of carbonate mineral component, exceeding 90% of the total composition based on ocular estimation. Diverse faunal assemblages of bivalves, ostracods, gastropods and conchostracans can be observed in the fossiliferous carbonate, including *Margaritifera*, *Darwinula* spp. and *Metacypris unibulla* (Xu et al., 2017). Although these bioclasts can occur in other FA as well, it differs in the very high proportion and maximum bioclast size in FA2. In thin sections, carbonate minerals are almost all dyed red by stain. The skeletal material and intergranular pores are filled within drusy and blocky sparry calcite (Fig. 4E-4G). Occasionally, silty quartz and feldspar grains oriented in the skeletal materials can be observed (Fig. 4H).

4.3. FA3

This FA is predominantly composed of the mixing of fossiliferous limestone (holding a domination) as well as minor clay-rich mudstone. FA3 contains several lithofacies types, resulting in creation of two subfacies associations (FA3a and FA3b). FA3a has been subdivided into two distinct lithofacies: LF6–Fossiliferous limestone with rhythmical and discontinuous mudstone interlaminations occurring between millimetre and multiple-centimetre intervals (Fig. 5A, B); and LF7–Interbedded fossiliferous limestone and clay-rich mudstone with

parallel-to-wavy bedding (Fig. 5C). Most of the bioclastic are unbroken in these two LF. The major difference is that fossiliferous limestone is dominant in LF6, while the proportions of two components are virtually the same in LF7. FA3b could also be further subdivided into two lithofacies: LF9–Mixing of fining-upward and scattered bivalve, ostracod shell fragments and mudstone component, with most of bioclastic convex upwards and broken; and LF10–Interbedded fossiliferous limestone and clay-rich mudstone with contorted bedding, slump structure and deformed lamination (Fig. 5D, E). In comparison to FA2, the proportion and size of bioclastic in FA3 are significantly reduced but there was no difference in biological species.

For limestone laminae, the matrix is commonly composed of clay minerals and minor amounts of silt-sized quartz (Fig. 5F, G). Minor visible intragranular dissolved pores and microfractures inside the bioclast can also be observed, revealed by SEM (Fig. 5H-5K). The mudstone component mainly consists of the mixing of clay minerals, carbonate minerals and silty siliceous grains, which are mostly black brown under plane-polarised observation. The bulk-rock XRD of 5 mudstone laminae samples reveal the average textural makeup as clay minerals (42.6%), carbonate minerals (31.9%), quartz (21.2%) and feldspar (4.4%) (Fig. 5L).

4.4. FA4

Two disparate subfacies associations (FA4a and FA4b) can be created in this FA to further analyse flow types and processes. FA4a consists of clay-rich mudstone with rhythmical and discontinuous fossiliferous

Fig. 4. Overview and examples of key features for FA2. (A) Fossiliferous carbonate with parallel-to-wavy bedding, primarily consisting of bivalve and ostracod shell fragments. Well X1, 3154.20 m; (B) Fossiliferous carbonate composed of randomly scattered bivalve and ostracod shell fragments. Well X1, 3106.75 m; (C) Fossiliferous carbonate with chaotic beddings. Well X1, 3160.00 m; (D) Calcified bioclasts are generally intact to broken. Well X1, 3192.80 m; (E) Carbonate minerals are almost all dyed red by stain. Elongate bioclastic occurs in randomly scattered distribution. Well X1, 3128.57 m, PPL; (F) Carbonate minerals are almost all dyed red by stain. Elongate bioclastic occurs in the slight imbrication distribution. Well X1, 3155.19 m, PPL; (G) Carbonate minerals are almost all dyed red by stain. Elongate bioclastic occurs in the imbrication distribution. Well X1, 3160.12 m, PPL; (H) Silty quartz and feldspar grains oriented in the elongate bioclastic. Well X1, 3191.94 m, PPL. PPL: plane-polarised light. (For interpretation of the references to colour in this figure legend, the reader is referred to the web version of this article.)

limestone interlaminations occurring between millimetre and multiple-centimetre intervals (LF8), which are dominated by parallel-to-wavy bedding (Fig. 6A). Rare lenses filled by bivalves and ostracod shell fragments can also be observed (Fig. 6B). FA4b corresponds to massive to faintly laminated mudstone containing fine floating bivalve and ostracod shell fragments (LF11) (Fig. 6C, D). In comparison to FA2 and FA3, the proportion and size of bioclastic in FA4 are further reduced. The proportion of bioclastic is in the range of 10 to 40% based on core observation and estimation. At the micron-scale, this FA is characterised by a homogeneous and high-proportion of clay-rich mudstone with a certain amount of calcified bioclasts (Fig. 6E-6H). Organic material is predominantly present as structured kerogen revealed by SEM, and carbonate nodules with organomineralic aggregates exist in a few samples (Fig. 6I, J). The bulk-rock XRD of 3 mudstone component samples reveal the average textural makeup as clay minerals (50.5%), quartz (25.8%), carbonate minerals (18.4%) and feldspar (5.4%) (Fig. 6K). Illite (averaging around 40%) is the dominant clay mineral in FA4 (Fig. 6L).

4.5. FA5

FA5 is comprised of dark grey to black faintly millimetre-scale laminated mudstone and minor massive mudstone (LF12). Hand-sample observation reveals that this FA is commonly integrated monotonously, and no obvious grading trend and no deformed lamination can be observed (Fig. 7A-7D). Mineralogically, abundant silt-sized siliceous detrital grains are dispersed in the clay matrix in thin sections (Fig. 7E-7K). The mineral assemblage as determined from qualitative bulk-rock XRD analysis comprises clay minerals (58.6%), quartz (31.0%), feldspar (7.0%) and carbonate minerals (3.5%). Sparse pyrite grains show isolated distribution and are usually <10 μm in diameter. Clay minerals from qualitative XRD analysis reveal the average makeup as illite (41.1%), kaolinite (15.2%), chlorite (23.0%) and illite/smectite mixed layer (20.6%) (Fig. 7L, M). SEM characterisation reveals that the pore development is predominantly in the form of matrix pores preserved in areas of clay minerals (Fig. 7G-7K).
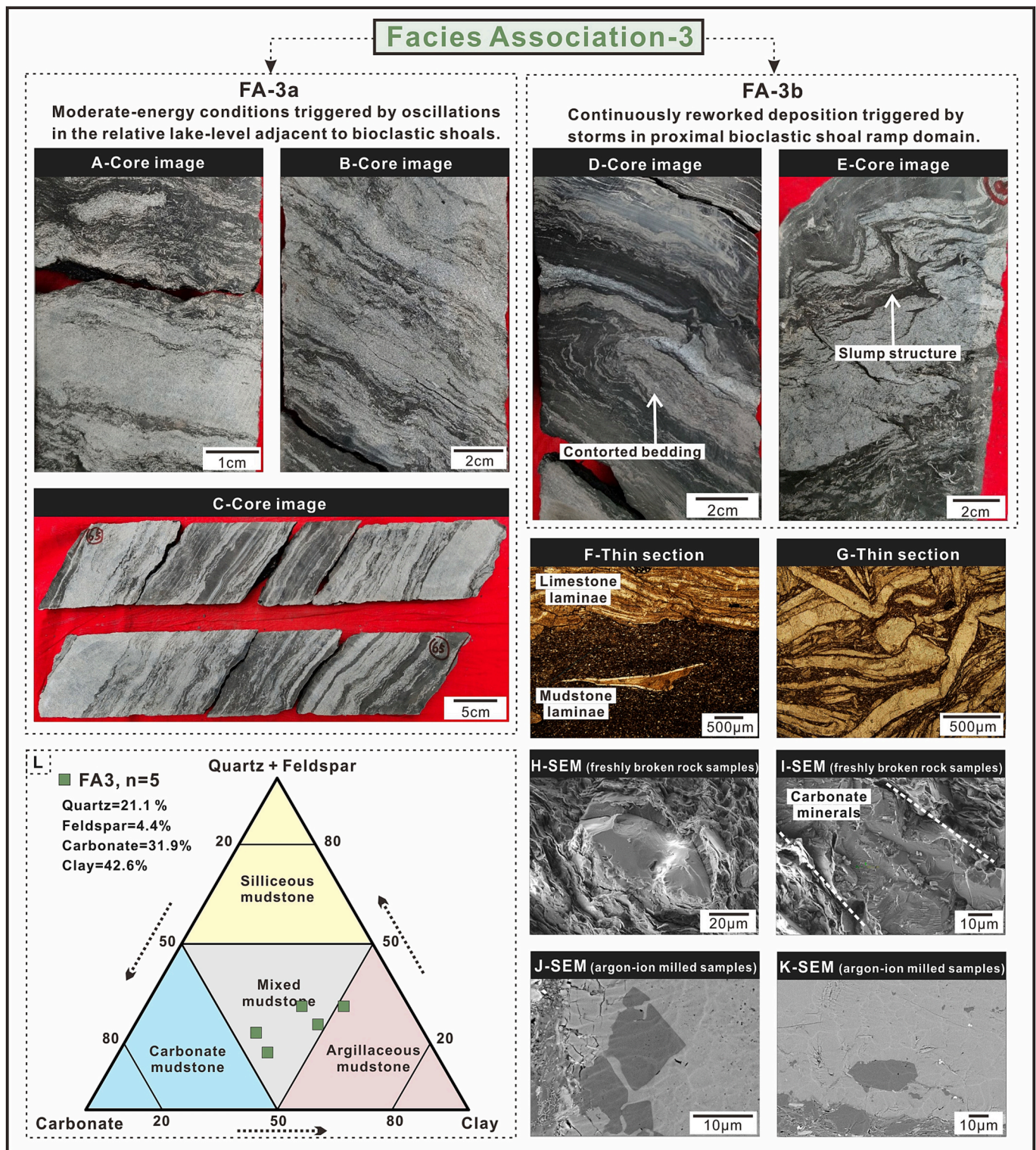
Fig. 5. Overview and examples of key features for FA3. (A) Fossiliferous carbonate with rhythmical and discontinuous mudstone interlaminations occurring between millimetre and multiple-centimetre intervals. Well X1, 3170.70 m; (B) Fossiliferous carbonate with rhythmical and discontinuous mudstone interlaminations occurring between millimetre and multiple-centimetre intervals. Well X1, 3195.10 m; (C) Interbedded fossiliferous limestone and clay-rich mudstone with parallel-to-wavy bedding. Well X1, 3194.90 m; (D) Interbedded fossiliferous limestone and clay-rich mudstone with contorted bedding. Well X1, 3143.10 m; (E) Interbedded fossiliferous limestone and clay-rich mudstone with slump structure and deformed lamination. Well X1, 3188.95 m; (F) The boundary between limestone and mudstone lamination. Well X1, 3151.80 m, PPL; (G) The matrix is commonly composed of clay minerals and minor amounts of silt-sized quartz. Well X1, 3198.30 m, PPL; (H) Microgranular calcite encased in flake clay minerals. Well X1, 3138.00 m, SEM; (I) Calcified bioclasts develops intergranular pores. Well X1, 3138.00 m, SEM; (J) Minor visible intragranular dissolved pores and microfracture inside the bioclast. Well X1, 3167.70 m, SEM; (K) Minor visible intragranular dissolved pores and microfracture inside the bioclast. Well X1, 3167.70 m, SEM. (L) Ternary diagrams of mineralogy in FA 3. PPL: plane-polarised light.
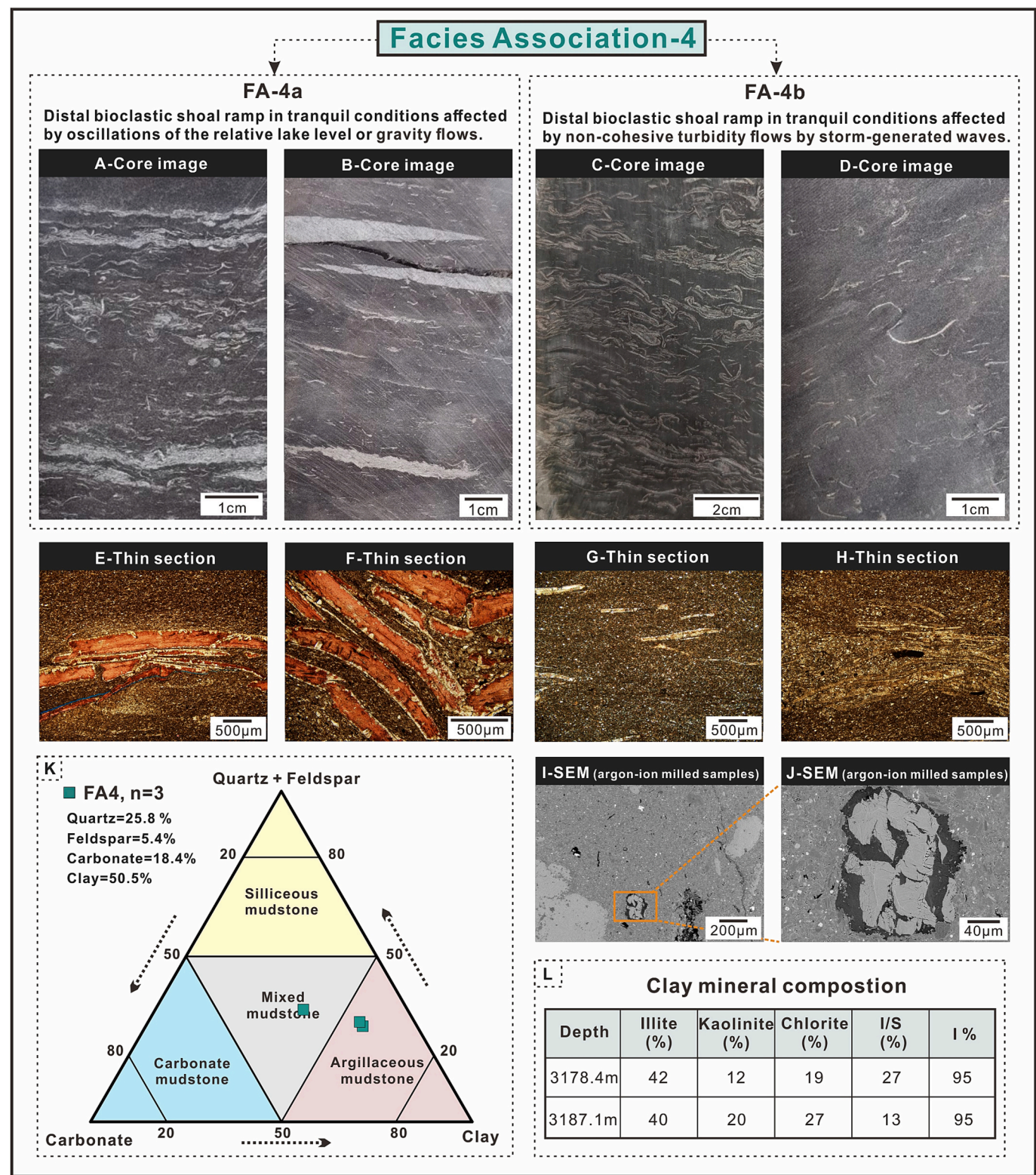
Fig. 6. Overview and examples of key features for FA4. (A) Clay-rich mudstone with rhythmical and discontinuous fossiliferous limestone interlaminations. Well X1, 3187.00 m; (B) Clay-rich mudstone with rhythmical and discontinuous fossiliferous limestone interlaminations. Well X1, 3169.00 m; (C) Faintly laminated mudstone containing fine floating bivalve, and ostracod shell fragments. Well X1, 3137.60 m; (D) Massive mudstone containing fine floating bivalve, and ostracod shell fragments. Well X1, 3184.00 m; (E) Bioclasts are mostly dispersed and separated with clay component. Well X1, 3157.22 m, PPL; (F) Bioclasts are arranged in a directional alignment. Well X1, 3157.22 m, PPL; (G) Homogeneous and high-proportion clay-rich mudstones with minor calcified bioclasts. Well X1, 3183.44 m, PPL; (H) Calcified bioclasts are oriented in clay-rich mudstones. Well X1, 3183.44 m, PPL; (I) The rock is mainly composed of clay minerals and siliceous minerals, accompanied by a small amount of carbonate minerals. Well X1, 3178.38 m, SEM; (J) Local magnification of (I). Microgranular calcite is alternately distributed organic matter. Well X1, 3178.38 m, SEM; (K) Ternary diagrams of mineralogy in FA4; (L) XRD results of two typical FA4 samples show that illite is the main component of clay minerals. PPL: plane-polarised light.
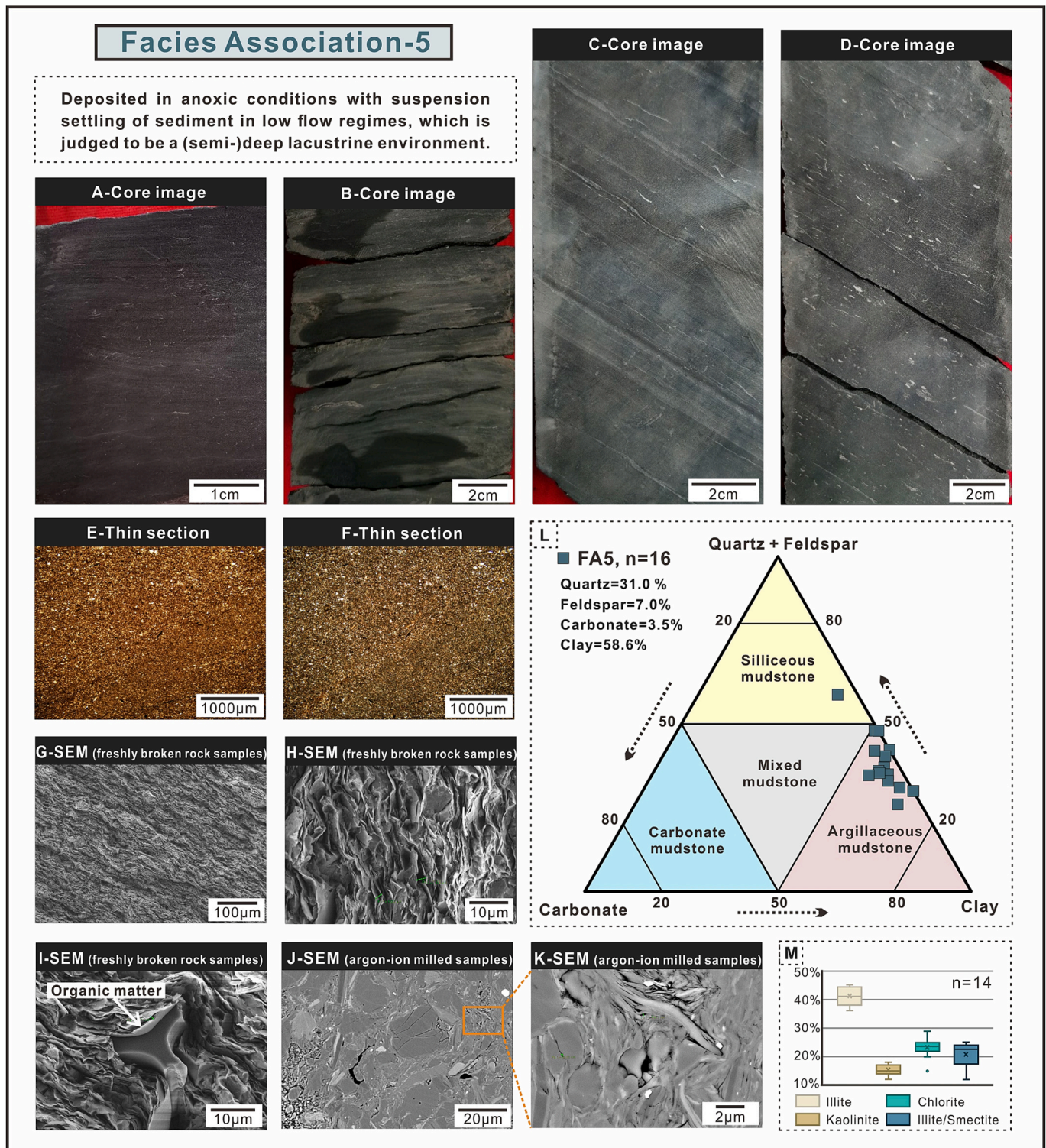
Fig. 7. Overview and examples of key features for FA5. (A) Grey-black massive mudstone. Well X1, 3167.00 m; (B) Dark grey faintly millimetre-scale laminated mudstone. Well X1, 3136.00 m; (C) Dark grey faintly millimetre-scale laminated mudstone. Well X1, 3194.50 m; (D) Dark grey faintly millimetre-scale laminated mudstone. Well X1, 3200.80 m; (E) Under PPL and (F) under XPL are from the same location within a thin section. The rock is commonly integrated monotonously and no obvious grading trend and no deformed lamination can be observed. Well X1, 3165.44 m; (G) Matrix pores preserved in areas of clay minerals, which is oriented parallel to bedding. Well X1, 3142.60 m, SEM; (H) Matrix pores preserved in areas of clay minerals, which is oriented parallel to bedding. Well X1, 3147.75 m, SEM; (I) Organic matter is encapsulated in matrix pores. Well X1, 3142.60 m, SEM; (J) The rock is dominated by clay minerals and siliceous minerals. Well X1, 3147.75 m, SEM; (K) Local magnification of (J). Matrix pores preserved in areas of clay minerals. Well X1, 3147.75 m, SEM; (L) Ternary diagrams of mineralogy in FA5; (M) XRD results of 15 typical FA5 samples show that illite is the main component of clay minerals. PPL, plane-polarised light; XPL, cross-polarised light. Refer to Appendix B for all sample information.

5. Bulk-rock organic geochemical data of mudstone component

The TOC data from Well X1 and Well X3 vary between 0.41 wt% and 3.29 wt%, with an average of 1.37 wt% ($n = 99$). For Well X1, FA1 (0.78 to 1.10 wt%; mean: 0.93 wt%) and FA2 (0.41 to 1.75 wt%; mean: 0.87 wt%) contain relatively low TOC. FA3 (0.60 to 2.08 wt%; mean: 1.33 wt%) and FA4 (0.70 to 2.63 wt%; mean: 1.41 wt%) are characterised by relatively middle TOC. In contrast, FA5 (0.83 to 3.29 wt%; mean: 1.55 wt%) contains relatively high TOC. TOC distribution characteristics of different FA in Well X3 are similar to those in Well 1 (Fig. 8).

The T_{max} values mainly fell in the range of 450 °C to 470 °C (458 °C on average) in Well X3. However, the J_1dn samples of Well X1 are now buried to a depth of >3000 m, and have the higher T_{max} values, ranging from 480 °C to 520 °C (502 °C on average). The cross plot of the HI values versus T_{max} proposed by Hunt (1995) reveals that most of the samples in Well X3 fall within the field of Type II kerogen (Fig. 9).

6. Facies associations distribution and stratigraphic correlation

Facies associations stacking patterns and standard gamma ray (SGR) were both used to distinguish cyclicities in this study. SGR reflects the signal of the element potassium (e.g. potassium feldspar, mica and illite), thorium and uranium. In general, computed gamma ray (CGR, omitting the uranium) are usually used to reflect the variation of terrestrial input (Fairbanks et al., 2016; Peng, 2021). Considering the general low amount of potassium feldspar in the study area as deduced from XRD analysis (Appendix B), the summation of potassium sources is sensitive to detrital clay content. Therefore, in situations without CGR, SGR can be used as a proxy reflecting the variation in terrestrial clay mineral input (Wei and Swennen, 2022). The increased SGR logs represents the increasing contribution of detrital clay mineral supply.

Based on facies associations stacking patterns and SGR logs, a total of six cycles can be distinguished, which can be further consolidated into three units throughout three-well stratigraphic correlation: the lower unit (composed of cycles 1 and 2); middle unit (composed of cycles 3 and 4); and upper unit (composed of cycles 5 and 6) (Fig. 10). At the bottom of each cycle, the SGR value starts at a lower level, then gradually increase upward of SGR, before finally change upward to decreasing SGR. Thus, each cycle, from the bottom to the top, represents an episodic process of enhancement and restoration of terrestrial clay mineral supply capacity. For the lower unit, the thickness of cycles 1 and 2 is relatively small, ranging from ca. 6 to 14 m in three-well stratigraphic correlation. There is no dominant FA in this unit, but rather a variety of FA change frequently vertically. This indicates that the lake-level fluctuations and sedimentary environment in this unit changed rapidly. For the middle unit, the thickness of cycles 3 and 4 is relatively large, ranging from ca. 20 to 32 m in three-well stratigraphic correlation. This unit is characterised by a high proportion of clay-rich facies associations

(FA4 and FA5) and a low proportion of carbonate-rich facies associations (FA2 and FA3). This feature is more significant in Well X2 and Well X3. For the upper unit, the thickness of cycles 5 and 6 is reduced, ranging from ca. 10 to 18 m in three-well stratigraphic correlation. Compared with unit 2, this unit is dominated by carbonate-rich facies associations (FA2 and FA3), while the proportion of clay-rich facies associations (FA4 and FA5) is greatly reduced.

Therefore, in the bottom-up stratigraphic correlation, J_1dn has the characteristic of 'frequent intermixing of multiple FA' → 'FA4 + FA5 predominates' → 'FA2 + FA3 predominates'.

7. Discussion

7.1. Depositional processes of each facies association

FA1: The siltstone laminae are interpreted to be related to traction plus fallout processes from waning turbulent flows with high suspended loads (Sumner et al., 2008; Zavala et al., 2011). The sharp within-bed scour in siltstone laminae reflects sudden increasing discharge events (Bhattacharya and MacEachern, 2009). Minor soft sediment deformation of siltstone laminae indicates episodic high sedimentation rates atop unsaturated mudstone layers (Mulder et al., 2003; Bhattacharya and MacEachern, 2009; Birgenheier et al., 2017; DeReuil and Birgenheier, 2018). Siliceous siltstone overlain by mudstone laminae indicate that these deposits are the result of episodic sediment delivery as the flow deceased (Edwards et al., 2005; Trabucho-Alexandre, 2014; DeReuil and Birgenheier, 2018). Therefore, the presence of both siltstone and mudstone laminae can be interpreted as the result of variations in discharge from a fluvial source supplying sediment to the lacustrine system for prolonged periods derived from weathering of available sediment source (Plink-Björklund and Steel, 2004). Silt deposition may occur during an increased flow stage, and the mud deposition may have formed during a decreasing flow stage (Ebinghaus et al., 2014; Cui et al., 2022). Mottled texture and subjacent burrows inside the mudstone intervals were likely deposited via the same mechanisms due to contemporaneous colonisation by burrowers (Bhattacharya and MacEachern, 2009). Burrowing organisms may colonise without the stressors of freshwater input or high sediment loads during bioturbation. Accordingly, this FA is inferred as having been deposited at the distal delta front as well as shallow lacustrine without being affected by bio-carbonate deposition.

FA2: This FA is confined to local carbonate sources controlled by bio-carbonate deposition. The bio-carbonate deposition occurs commonly in persistently agitated high-energy environments subject to frequent wave action above the normal wave base (Rivera et al., 2018). The abundance of bivalve genus *Margaritifera* and ostracod faunal assemblages *Darwinula* spp. and *Metacypris unibulla* indicates not only a freshwater lacustrine environment, but also from a late Early Jurassic
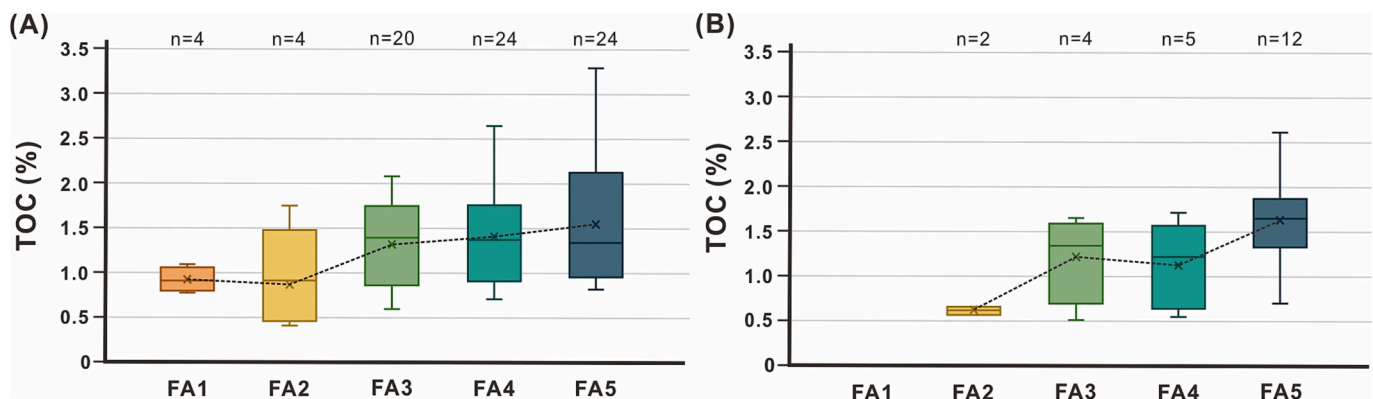
Fig. 8. Box and whisker plots showing total organic carbon (TOC) values of different FA. The data from Well X1 and Well X3 have similar patterns: FA1 and FA2 contain relatively low TOC. FA3 and FA4 are characterised by relatively middle TOC. In contrast, FA5 contains relatively high TOC. (A) Well X1; (B) Well X3.
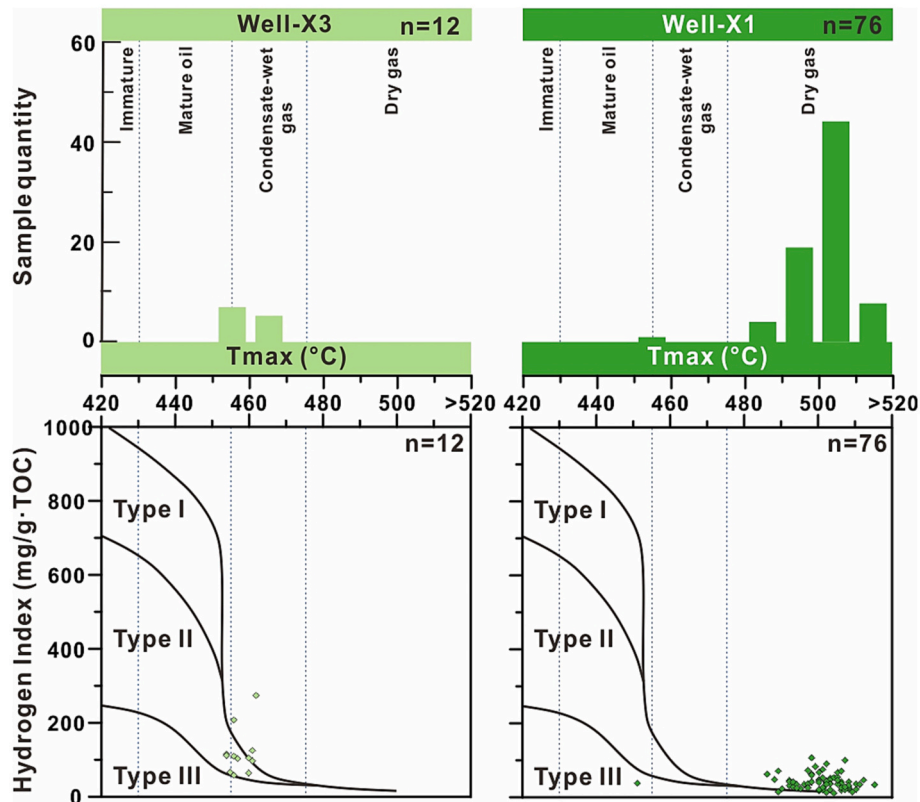
Fig. 9. Histograms of Tmax and HI (mg/g·TOC) versus Tmax (°C) of the studied samples in 2 wells derived from Rock-Eval pyrolysis. In Well X3, analyses of rock-eval demonstrated that the kerogens are predominantly Type II. Thermally overmature (Tmax>480 °C) of kerogen in Well X1 obfuscates the evaluations of organic matter sources.
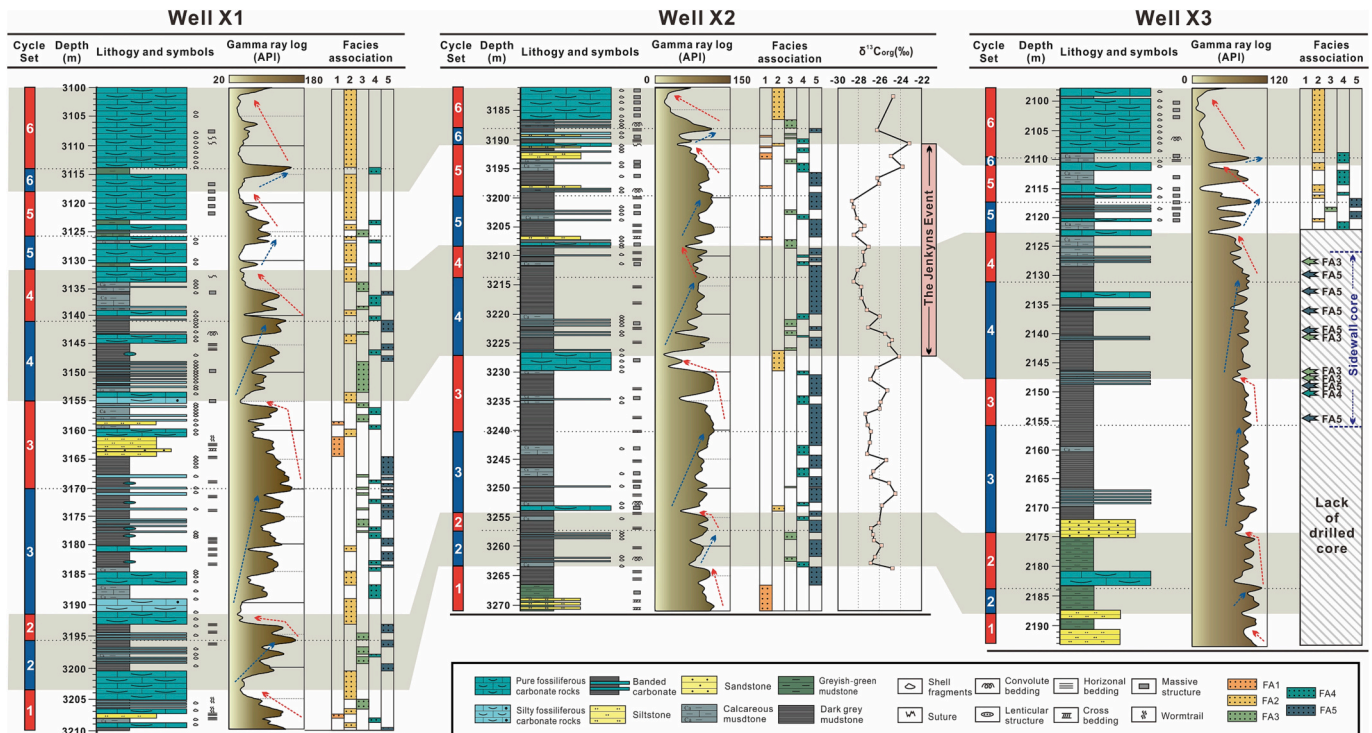
Fig. 10. Stratigraphic correlation of three drilled wells in the J$_1$dn, Sichuan Basin. This section shows the cycle set, lithology, standard gamma ray, and vertical transitions of FA. In this sequence, the vertical transitions of FA form a complete lacustrine transgressive-regressive sedimentary cycle. FA2 is mainly distributed at the Upper and Lower J$_1$dn, while FA4 and FA5 are mainly distributed at the Middle J$_1$dn. The organic carbon isotope data of Well X2 came from Liu et al. (2020a). Refer to Appendix B for all sample information.

age (Xu et al., 2017). Most fossiliferous limestone exhibit parallel-to-wavy bedding (LF4), indicating the fast bio-carbonate deposition in relative tranquil lake wave conditions. Furthermore, the mid-palaeolatitude setting and geomorphology (surrounding orogenic belts towards the northwest and adjoining oceans towards the southeast) of the palaeo-Sichuan Basin would have exposed itself to a monsoonal climate (Xu et al., 2017), which is conducive to storm and hurricane events (refer to the present-day Pacific Northwest summer monsoon; Chandler et al., 1992; Bjerrum et al., 2001). Therefore, the chaotic bedding with randomly scattered of bioclastic (LF5) is interpreted as fast bio-carbonate deposition probably in-situ remobilised, resuspended and redeposited by storms. Silty terrigenous clastic grains observed in the skeletal materials may be interpreted as the transport process via storms to the bioclastic shoals (Spalletti et al., 2001; Bádenas and Aurell, 2001). Accordingly, this FA is inferred as having been deposited at accretionary bioclastic shoals in a warm, well-oxygenated fresh water above to the normal wave base (Martini et al., 2007), sometimes affected by storm events or intensive lake wave action.

FA3: The parallel-to-wavy bedding in FA3a is interpreted as having been generated by oscillatory lake waves with relatively tranquil conditions (Rivera et al., 2018). By comparison, the fossiliferous limestone laminae are more inclined to form in a bioclastic shoal ramp domain above the wave base (Rivera et al., 2018), while rhythmical and discontinuous mudstone interlaminations are interpreted as the deposition from suspension fall out of clay-rich terrigenous clastic near or below the wave base (Sami and Desrochers, 1992). Therefore, the environment of FA3a is characterised by moderate-energy conditions triggered by oscillations in the relative lake-level adjacent to bioclastic shoals (Spalletti et al., 2001).

LF9 and LF10 are grouped into the FA3b due to their remobilised, resuspended or redeposited characteristics revealed by the hand sample observation. Storm-waves would exert cyclic loading stress on the lake floor, inducing to-and-fro motion and the redeposition of bioclasts as well as clay-rich mudstone (Cowan and James, 1992; Bouchette et al., 2001). The massive and mud-supported textures together with fining-upward and scattered bivalve, ostracod shell fragment (LF9) represents deposition during the waning phases of storm-generated turbulent flows (Sami and Desrochers, 1992; Spalletti et al., 2001; Bádenas and Aurell, 2001; Martini et al., 2007). In addition, with progressive consolidation of deposits, the high-cohesion lime/mud laminae may produce various deformation structures triggered by episodic high-energy storms, such as contorted bedding, slump structure and escape structures (LF10) (Sami and Desrochers, 1992; Myrow et al., 2004; Chen et al., 2009). Therefore, the environment of FA3b is interpreted as continuously reworked deposition triggered by storms in a proximal bioclastic shoal ramp domain (Rivera et al., 2018).

FA4: The progressive decrease of bio-carbonate deposition and further increasing suspension settling of clay-rich terrigenous clastic indicates conditions more adjacent to the lake basin (Liang et al., 2018). The clay-rich mudstone with isolated discontinuous fossiliferous limestone interlaminations or lenses (LF8) can be interpreted as reflecting an intensive falling in lake level, resulting in small-scale in-situ bio-carbonate deposition reaching the distal domain of the ramp, or alternatively, deposition under gravity flows to disperse bioclastic towards the domain below the effective wave base (Wright et al., 2001; Macquaker et al., 2010; Ghadeer and Macquaker, 2011; Plint, 2013). Similarly, the depositional process of LF11 can be interpreted as the suspension accretion of minor content of floating bivalve, ostracod shell fragments and clay-rich mud below the storm wave base in a relatively low-energy environment (Rivera et al., 2018). These deposits may reflect the waning stages of non-cohesive turbidity flows by storm-generated waves (Shanmugam, 2008; Kietzmann et al., 2014). Accordingly, this FA is indicative of the development at the distal bioclastic shoal ramp domain that was intermittently influenced by storm events.

FA5: The presence of massive and weak parallel lamination indicates suspension settling in tranquil conditions. The moderate dark grey to black colour and occurrence of pyrite suggest an anoxic and suboxic environment (Paredes et al., 2009). Currents are inactive during deposition, as evidenced by the wide development of faintly laminated mudstone as well as the absence of unidirectional tractional structure (e.g. subtle erosional scours, ripple laminations) in FA5 (Macquaker et al., 2010; Birgenheier et al., 2017). The higher organic carbon suggests high primary productivity in the lacustrine surface during the deposition period (Liang et al., 2018). Accordingly, FA5 is identified as having been deposited in anoxic conditions with suspension settling of sediment in low flow regimes. Therefore, it is judged to be a (semi-)deep lacustrine environment.

7.2. Palaeolimnological change history of Sichuan Basin

The vertical transitions of FA and SGR logs reveal that J_1dn forms a complete lacustrine transgressive-regressive sedimentary cycle (Fig. 10). The interpreted evolution of the lacustrine depositional environment can be divided into three stages. While it is an idealised partitioning schemes and partial FA transitions are occasionally unintelligible, they provide guidance for a systematic interpretation of the depositional environment of the palaeo-Sichuan lacustrine basin.

7.2.1. Stage A (Cycles 1 and 2)

This stage corresponds to the depositional period of the bottom J_1dn, which is mainly composed of frequent intermixing of multiple FA at the Lower J_1dn. During this period, the Sichuan Basin was dominated by an accretionary bioclastic shoal environment in a warm, well-oxygenated fresh water as discussed above, but accompanied by frequent lake-level fluctuations.
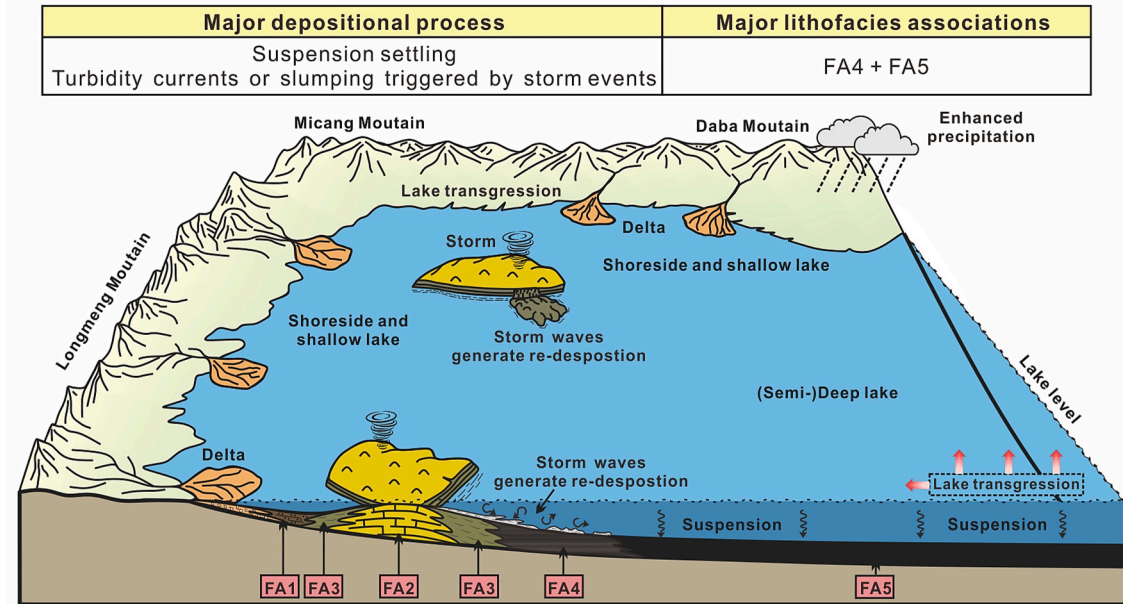
Before the deposition of the Lower J_1dn, lacustrine deposits of J_1m are characterised by interbedded mudstone and siltstone, and almost no bioclastic can be observed (Wang et al., 2020; Qiu and He, 2022). However, a mass of bioclasts were observed at the bottom J_1dn. Indeed, diverse faunal assemblages of bivalves, ostracods and gastropods already partially took hold in the palaeo-Sichuan Basin during the Early Toarcian, which is thought to be a precursor response during the Jenkyns Event (Vörös, 2005). Caswell and Coe (2013) suggest that the geologically rapid changes of biological species during the Toarcian were highly opportunistic, evidencing short lifespans, rapid generation times, and high juvenile recruitment. According to the view of Caswell and Coe (2013), strong environmental perturbations would decrease biodiversity but increase both the density and dominance of 'opportunists'. Thus, the widespread benthic communities in the Lower J_1dn were likely due to opportunistic species, and their population would increase rapidly under favourable environmental conditions (Levin et al., 2009), eventually leading to FA2 which occurred widely at this stage.

Therefore, it is likely that the palaeo-Sichuan lacustrine basin experienced a significant palaeolimnological or paleoclimatic perturbation during the transition from J_1m to J_1dn. Considering that the faunal assemblages in this stage were mainly composed of freshwater bivalves, ostracodes and gastropods (*Margaritifera*, *Darwinula* spp. and *Metacypris unibulla*) (Xu et al., 2017), the lake basin was likely transformed into a shallow lake environment with clear water and strong energy that probably experienced episodic eutrophication leading to biological flourishing.

7.2.2. Stage B (Cycles 3 and 4)

Based on the detailed FA interpretation, it was found that lacustrine transgression occurred during the depositional period of Stage B, leading to the deposition of clay-rich mudstone and the demise of bioclastic shoals. According to the recognition criteria, the Sichuan Basin during this stage was dominated by the proximal/distal bioclastic shoal ramp (in tranquil conditions that were at times affected by storm-induced waves or oscillatory currents) or a (semi-)deep lacustrine environment. Overall, at this stage the lake level was at a relative highstand

(A) Lacustrine-level highstand

Major depositional process	Major lithofacies associations
Suspension settling Turbidity currents or slumping triggered by storm events	FA4 + FA5

(B) Low relative lacustrine level

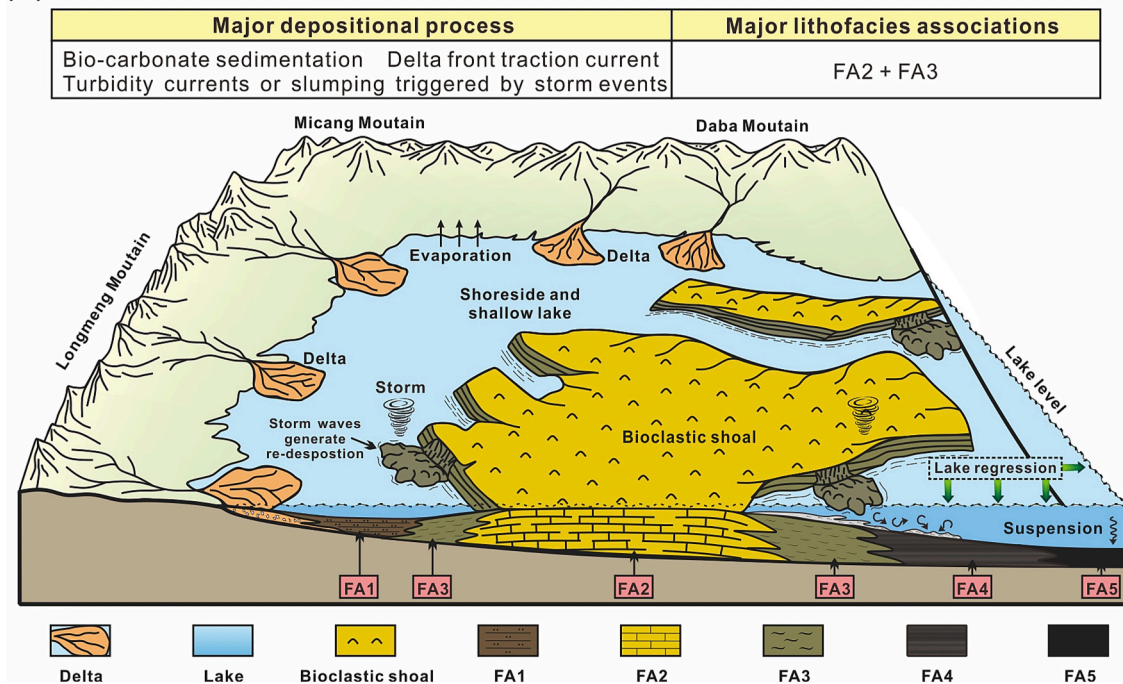| Major depositional process	Major lithofacies associations
Bio-carbonate sedimentation Delta front traction current Turbidity currents or slumping triggered by storm events	FA2 + FA3

Fig. 11. Schematic three-dimensional diagrams illustrating the synthesis lacustrine depositional environment model of J_1dn in Sichuan Basin affected by the Jenkyns Event. This model can be divided into two parts: (A) Lacustrine-level highstand stage, which is characterised by a proximal/distal bioclastic shoal ramp or a (semi-) deep lacustrine environment; (B) Lacustrine-level lowstand stage, which is characterised by the recovery of bioclastic shoals.

(Fig. 11A).

This stage coincided with the initiation of the Jenkyns Event, with significant CIE features observed in organic-rich sediments in Well X2 (Fig. 10 and Appendix B) (Liu et al., 2020a). There are several possible mechanisms independently or collectively driving the short-lived demise of fossiliferous carbonate. The Jenkyns Event is characterised by global persisting elevated temperatures (Bailey et al., 2003; Ullmann et al., 2020), which would promote the evaporation of the approaching marine waters adjacent to the Sichuan Basin (Xu et al., 2017). Affected by the monsoonal climate and the paleogeomorphology around the palaeo-Sichuan Basin, the steamy vapours would accumulate in the

interior of the lacustrine basin and promote precipitation. Continuing precipitation and global warming would lead to a rapid lacustrine-level rise and the increasing availability of accommodation space for sediments. Therefore, these unfavorable conditions severely limited the living environment of benthic communities. In addition, the massive atmospheric p_{CO2} during the Jenkyns Event may also have increased acidity of the lake water and lead to the carbonate crisis (Kleypas et al., 1999; Gattuso and Buddemeier, 2000; Woodfine et al., 2008).

FA3, FA4 and FA5 were primarily affected by the rapid lacustrine-level rise. These fine-grained terrigenous components may originate from multiple sources, including windblown dust, fluvial processes or

volcanogenic materials (Reading and Richards, 1994). Combined with the stable tectonic background, these fine-grained components are more likely to have been transported and input into the lacustrine system by fluvial processes. These materials would stay in suspension for a long time, and accumulate by normal settling when the flow completely stopped (Zavala et al., 2011). However, the observations of FA3b and FA4b indicate that sediment transport and re-deposition in the study area were not negligible. As mentioned above, monsoonal atmospheric circulation dominated the climates of the palaeo-Sichuan lacustrine basin during this stage, which favoured the formation of short-lived and high-energy storms (Chandler et al., 1992; Sami and Desrochers, 1992; Léonide et al., 2011). The passage of storm-waves would exert a variety of loading stresses on the lake floor (Cowan and James, 1992; Bouchette et al., 2001). This process provided an efficient mechanism to transport coarse sediments and calcified bioclasts to the (semi-)deep lacustrine environments (Rivera et al., 2018). For fresh deposits, the weakly consolidated organo-minerallic aggregates with minor bioclastic could be readily re-suspended (Plint, 2013), and subsequently settled down due to gravity during the quiescent period, thus forming LF9 and LF11. For semi-consolidated deposits, the cyclic stress triggered by episodic high-energy storms would more likely lead to mechanical rupture or deformation, thus forming LF10 (Sami and Desrochers, 1992; Myrow et al., 2004). Therefore, the storm and hurricane events allowed the mixing of fossiliferous carbonate and clay-rich mudstone in the lacustrine system.

Another notable feature of this stage is the extensive accumulation of organic matter. In a (semi-)deep lacustrine environment, the comminuted higher plant derived macerals and amorphous organic matter can be observed by SEM (Fig. 7I). As discussed above, continuing precipitation and global warming during the Jenkyns Event would lead to the enhanced terrestrial influx and rapid lacustrine-level rise. This process may lead to the subsequent development of eutrophication and deoxygenation (Them et al., 2017). On the one hand, under such hydrologic conditions, planktonic microfauna would flourish and sequestrate isotopically light CO_2 from the atmospheric circulation via photosynthesis (Gorham et al., 1974). On the other hand, as precipitation and terrestrial influx greatly increased during the lake-level highstand stage, the large amount of dissolved and undissolved organic carbon would be exported by streams from forested catchments to lakes. Eventually, the organic carbon would be widely sequestered in the lake sediment pool.

7.2.3. Stage C (Cycles 5 and 6)

This stage corresponds to the Upper J_1dn, mainly composed by FA2 and recovering the depositional environment dominated by bioclastic shoals. As proven by the thicker and higher proportion of FA2, the thickness and planar distribution of bioclastic shoals in Stage C should be greater than that of Stage A (Fig. 10). Overall, the lake level is at a relative lowstand at this stage (Fig. 11B).

Towards the end of the Jenkyns Event, a series of responses to earth system (e.g. the recovery of carbonate production, reduction of organic carbon accumulation, recovery of carbon isotope, enhancement of wildfire) captures the enhancement of p_{O_2} in the atmosphere and the water, and the reduction in global temperature (Hesselbo et al., 2007; Léonide et al., 2011; Baker et al., 2017). Regarding the palaeo-Sichuan lacustrine basin, the FA transition from semi-deep lake to bioclastic shoals indicates the lake regression. Therefore, as lake levels fell and oxygen levels increased, faunal assemblages of bivalves, ostracods and gastropods that colonised the basin floor would regain dominance. Moreover, during this time, global palaeoclimatic conditions are thought to have gradually dried (Dera et al., 2009; Korte et al., 2015; Baker et al., 2017). These favourable conditions jointly promoted the recovery of bioclastic shoals. A large number of silty terrigenous clastic grains at this stage would be transported into the lake basin in the form of traction flow or gravity flow, which would inevitably dilute the distribution of organic matter (Wei and Swennen, 2022), and establish conditions unfavorable to the accumulation and preservation of organic matter.

8. Conclusions

The fossiliferous carbonate and clay-rich mudstone samples of J_1dn, palaeo-Sichuan lacustrine basin, offers an exceptional opportunity to evaluate lacustrine environment evolution during the Toarcian. Detailed lithofacies descriptions and interpretations from J_1dn reveal a mixed siliciclastic-carbonate setting. This lacustrine depositional system displays considerable facies variability and complexity both laterally and vertically and can be delineated into five FA: (FA1) volumetrically dominated by frequently interbedded siltstones and mudstones interpreted as the distal delta front and shallow lacustrine; (FA2) a diverse suite of calcified bioclast deposits interpreted as bioclastic shoals; (FA3) predominantly composed of the mixing of fossiliferous limestone and minor clay-rich mudstone interpreted as a proximal bioclastic shoal ramp; (FA4) clay-rich mudstone with rhythmical and discontinuous fossiliferous limestone laminated or fine floating bivalve and ostracod shell fragments interpreted as a distal bioclastic shoal ramp; and (FA5) dark grey to black mudstone interpreted as a (semi-)deep lacustrine environment.

The vertical transitions of FA form a complete lacustrine transgressive-regressive sedimentary cycle. The interpreted evolution of the lacustrine depositional environment can be divided into three stages during the Toarcian stage, which is believed to be controlled by lacustrine-level fluctuation: Stage A (mainly an accretionary bioclastic shoal environment in warm, well-oxygenated fresh water, but accompanied by frequent lake-level fluctuations); Stage B (mainly a deep lacustrine environment at the relative lake-level highstand, occasionally affected by storm-induced waves); and Stage C (recovering the depositional environment dominated by bioclastic shoals at the relative lake-level lowstand). During the Stages A and C, 'opportunists' (bivalves, ostracods and gastropods) evidenced rapid population increases in the Upper and Lower J_1dn sediments, which may be attributed to associated environmental perturbations during the Jenkyns Event. In contrast, a significant increase in the proportion of FA5 into the Stage B indicates intensive lacustrine transgression, resulting in clay-rich lithofacies to depositing sediment by suspension settling and turbidity currents. At different stages, storm and hurricane events would induce the remobilised, resuspended and redeposit of unconsolidated sediments, allowing the mixing of fossiliferous carbonate and clay-rich mudstone in the lacustrine system. Finally, this article establishes the depositional environment evolution model at the lake-level highstand stage and lowstand stage of the palaeo-Sichuan lacustrine basin contemporaneous with the Jenkyns Event, which has implications for the evaluation of other Toarcian lacustrine systems.

Declaration of Competing Interest

We declare that we do not have any conflict of interest in connection with the work submitted.

Data availability

The data that supports the findings of this study are available in the supplementary materials of this article.

that greatly enhanced the manuscript.

Appendix A. Supplementary data

Supplementary data to this article can be found online at https://doi.org/10.1016/j.palaeo.2023.111841.

References

Ahokas, J.M., Nystuen, J.P., Martinius, A.W., 2014. Stratigraphic signatures of punctuated rise in relative sea-level in an estuary-dominated heterolithic succession: incised valley fills of the Toarcian Ostrealv Formation, Neill Klinter Group (Jameson Land, East Greenland). Mar. Petrol. Geol. 50, 103–129.

Bádenas, B., Aurell, M., 2001. Proximal–distal facies relationships and sedimentary processes in a storm dominated carbonate ramp (Kimmeridgian, northwest of the Iberian Ranges, Spain). Sed. Geol. 139, 319–340.

Bailey, T.R., Rosenthal, Y., McArthur, J.M., van de Schootbrugge, B., Thirlwall, M.F., 2003. Paleoceanographic changes of the late Pliensbachian-early Toarcian interval: a possible link to the genesis of an Oceanic Anoxic Event. Earth Planet. Sci. Lett. 212, 307–320.

Baker, S.J., Hesselbo, S.P., Lenton, T.M., Duarte, L.V., Belcher, C.M., 2017. Charcoal evidence that rising atmospheric oxygen terminated early Jurassic Ocean anoxia. Nat. Commun. 8.

Bhattacharya, J.P., MacEachern, J.A., 2009. Hyperpycnal rivers and prodeltaic shelves in the cretaceous Seaway of North America. J. Sed. Res. 79, 184–209.

Birgenheier, L.P., Horton, B., McCauley, A.D., Johnson, C.L., Kennedy, A., 2017. A depositional model for offshore deposits of the lower Blue Gate Member, Mancos Shale, Uinta Basin, Utah, USA. Sedimentology 64, 1402–1438.

Bjerrum, C.J., Surlyk, F., Callomon, J.H., Slingerland, R.L., 2001. Numerical paleoceanographic study of the early Jurassic transcontinental Laurasian Seaway. Paleoceanography 16, 390–404.

Bouchette, F., Seguret, M., Moussine-Pouchkine, A., 2001. Coarse carbonate breccias as a result of water-wave cyclic loading (uppermost Jurassic–South-East Basin, France). Sedimentology 48, 767–789.

Boulila, S., Galbrun, B., Huret, E., Hinnov, L.A., Rouget, I., Gardin, S., Bartolini, A., 2014. Astronomical calibration of the Toarcian Stage: implications for sequence stratigraphy and duration of the early Toarcian OAE. Earth Planet. Sci. Lett. 386, 98–111.

Cai, C., Worden, R.H., Bottrell, S.H., Wang, L., Yang, C., 2003. Thermochemical sulphate reduction and the generation of hydrogen sulphide and thiols (mercaptans) in Triassic carbonate reservoirs from the Sichuan Basin, China. Chem. Geol. 202, 39–57.

Caswell, B.A., Coe, A.L., 2013. Primary productivity controls on opportunistic bivalves during early Jurassic oceanic deoxygenation. Geology 41, 1163–1166.

Chandler, M.A., Rind, D., Ruedy, R., 1992. Pangaean climate during the early Jurassic: GCM simulations and the sedimentary record of paleoclimate. Geol. Soc. Am. Bull. 104, 543–559.

Chen, J., Chough, S., Chun, S., Han, Z., 2009. Limestone pseudoconglomerates in the late Cambrian Gushan and Chaomidian Formations (Shandong Province, China): soft-sediment deformation induced by storm-wave loading. Sedimentology 56, 1174–1195.

Chen, S., Zhang, H., Lu, J., Yang, Y., Liu, C., Wang, L., Zou, X., Yang, J., Tang, H., Yao, Y., Huang, Y., Ni, S., Chen, Y., 2015. Controlling factors of Jurassic Da'anzhai Member tight oil accumulation and high production in Central Sichuan Basin, SW China. Petrol. Explor. Dev. 42, 206–214.

Cohen, A.S., Coe, A.L., Harding, S.M., Schwark, L., 2004. Osmium isotope evidence for the regulation of atmospheric CO2 by continental weathering. Geology 32, 157.

Cowan, C., James, N., 1992. Diastasis cracks: mechanically generated synaeresis-like cracks in Upper Cambrian shallow water oolite and ribbon carbonates. Sedimentology 39, 1101–1118.

Cui, H., Zhu, S., Tan, M., Tong, H., 2022. Depositional and diagenetic processes in volcanic matrix-rich sandstones from the Shanxi and Shihezi Formations, Ordos Basin, China: Implication for volcano-sedimentary systems. Basin Res. 34, 1859–1893.

Danise, S., Twitchett, R.J., Little, C.T.S., 2015. Environmental controls on Jurassic marine ecosystems during global warming. Geology 43, 263–266.

Dera, G., Pellenard, P., Neige, P., Deconinck, J.F., Pucéat, E., Dommergues, J.L., 2009. Distribution of clay minerals in early Jurassic Peritethyan seas: palaeoclimatic significance inferred from multiproxy comparisons. Palaeogeogr. Palaeoclimatol. Palaeoecol. 271, 39–51.

DeReuil, A.A., Birgenheier, L.P., 2018. Sediment dispersal and organic carbon preservation in a dynamic mudstone-dominated system, Juana Lopez Member, Mancos Shale. Sedimentology 66, 1002–1041.

Duncan, R.A., Hooper, P.R., Rehacek, J., Marsh, J.S., Duncan, A.R., 1997. The timing and duration of the Karoo igneous event, southern Gondwana. J. Geophys. Res. Solid Earth 102, 18127–18138.

Ebinghaus, A., Hartley, A.J., Jolley, D.W., Hole, M., Millett, J., 2014. Lava-sediment interaction and drainage-system development in a large igneous province: Columbia River Flood Basalt Province, Washington State, U.S.A. J. Sed. Res. 84, 1041–1063.

Edwards, C.M., Hodgson, D.M., Flint, S.S., Howell, J.A., 2005. Contrasting styles of shelf sediment transport and deposition in a ramp margin setting related to relative sea-level change and basin floor topography, Turonian (Cretaceous) Western Interior of central Utah, USA. Sed. Geol. 179, 117–152.

Fairbanks, M.D., Ruppel, S.C., Rowe, H., 2016. High resolution stratigraphy and facies architecture of the Upper cretaceous (Cenomanian–Turonian) Eagle Ford Group, Central Texas Eagle Ford Stratigraphy and Facies Architecture. AAPG Bull. 100, 379–403.

Feng, R., Wu, Y., Tao, S., Zhang, T., Yue, T., Yang, J., Liu, M., 2015. Sedimentary microfacies characteristics and their control on reservoirs in Da'anzhai Member, lower Jurassic, Sichuan Basin. Petrol. Geol. Experiment. 37, 320–328 (in Chinese with English abstract).

Gattuso, J.P., Buddemeier, R.W., 2000. Calcification and CO2. Nature 407, 311–313.

Ghadeer, S.G., Macquaker, J.H.S., 2011. Sediment transport processes in an ancient mud-dominated succession: a comparison of processes operating in marine offshore settings and anoxic basinal environments. J. Geol. Soc. 168, 1121–1132.

Gorham, E., Lund, J.W., Sanger, J.E., Dean, W.E., 1974. Some relationships between algal standing crop, water chemistry, and sediment chemistry in the English Lakes. Limnol. Oceanogr. 19, 601–617.

Harries, P.J., Little, C.T.S., 1999. The early Toarcian (Early Jurassic) and the Cenomanian-Turonian (Late Cretaceous) mass extinctions: similarities and contrasts. Palaeogeogr. Palaeoclimatol. Palaeoecol. 54, 39–66.

Hermoso, M., Le Callonnec, L., Minoletti, F., Renard, M., Hesselbo, S.P., 2009. Expression of the early Toarcian negative carbon-isotope excursion in separated carbonate microfractions (Jurassic, Paris Basin). Earth Planet. Sci. Lett. 277, 194–203.

Hermoso, M., Minoletti, F., Rickaby, R.E.M., Hesselbo, S.P., Baudin, F., Jenkyns, H.C., 2012. Dynamics of a stepped carbon-isotope excursion: Ultra high-resolution study of early Toarcian environmental change. Earth Planet. Sci. Lett. 319–320, 45–54.

Hesselbo, S.P., Jenkyns, H.C., Duarte, L.V., Oliveira, L.C.V., 2007. Carbon-isotope record of the early Jurassic (Toarcian) Oceanic Anoxic Event from fossil wood and marine carbonate (Lusitanian Basin, Portugal). Earth Planet. Sci. Lett. 253, 455–470.

Hunt, J.M., 1995. Petroleum Geochemistry and Geology. In: 2nd ed. W.H. Freeman and Company, San Francisco, p. 201 p..

Jenkyns, H.C., 2010. Geochemistry of oceanic anoxic events. Geochem. Geophys. Geosyst. 11.

Jin, X., Shi, Z., Baranyi, V., Kemp, D.B., Han, Z., Luo, G., Hu, J., He, F., Chen, L., Preto, N., 2020. The Jenkyns Event (early Toarcian OAE) in the Ordos Basin, North China. Global Planet. Change 193, 103273.

Kafousia, N., Karakitsios, V., Mattioli, E., Kenjo, S., Jenkyns, H.C., 2014. The Toarcian oceanic anoxic event in the Ionian Zone, Greece. Palaeogeogr. Palaeoclimatol. Palaeoecol. 393, 135–145.

Kietzmann, D.A., Palma, R.M., Riccardi, A.C., Martín-Chivelet, J., López-Gómez, J., 2014. Sedimentology and sequence stratigraphy of a Tithonian-Valanginian carbonate ramp (Vaca Muerta Formation): a misunderstood exceptional source rock in the southern Mendoza area of the Neuquén Basin. Argentina. Sed. Geol. 302, 64–86.

Kleypas, J.A., Buddemeier, R.W., Archer, D., Gattuso, J.P., Langdon, C., Opdyke, B.N., 1999. Geochemical consequences of increased atmospheric carbon dioxide on coral reefs. Science 284, 118–120.

Korte, C., Hesselbo, S.P., Ullmann, C.V., Dietl, G., Ruhl, M., Schweigert, G., Thibault, N., 2015. Jurassic climate mode governed by ocean gateway. Nat. Commun. 6.

Krencker, F.N., Lindström, S., Bodin, S., 2019. A major sea-level drop briefly precedes the Toarcian oceanic anoxic event: Implication for Early Jurassic climate and carbon cycle. Sci. Rep. 9.

Lazar, O.R., Bohacs, K.M., Macquaker, J.H., Schieber, J., Demko, T.M., 2015. Capturing key attributes of fine-grained sedimentary rocks in outcrops, cores, and thin sections: Nomenclature and description guidelines. J. Sed. Res. 85, 230–246.

Léonide, P., Floquet, M., Durlet, C., Baudin, F., Pittet, B., Lécuyer, C., 2011. Drowning of a carbonate platform as a precursor stage of the early Toarcian global anoxic event (Southern Provence sub-Basin, South-east France). Sedimentology 59, 156–184.

Levin, L.A., Ekau, W., Gooday, A.J., Jorissen, F., Middelburg, J.J., Naqvi, S.W.A., Neira, C., Rabalais, N.N., Zhang, J., 2009. Effects of natural and human-induced hypoxia on coastal benthos. Biogeosciences 6, 2063–2098.

Li, Y., Feng, Y., Liu, H., Zhang, L., Zhao, S., 2013. Geological characteristics and resource potential of lacustrine shale gas in the Sichuan Basin, SW China. Petrol. Explor. Dev. 40, 454–460.

Liang, C., Jiang, Z., Cao, Y., Wu, J., Wang, Y., Hao, F., 2018. Sedimentary characteristics and origin of lacustrine organic-rich shales in the Salinized Eocene Dongying Depression. Geol. Soc. Am. Bull. 130, 154–174.

Liu, J., Cao, J., He, T., Liang, F., Pu, J., Wang, Y., 2022. Lacustrine redox variations in the Toarcian Sichuan Basin across the Jenkyns Event. Glob. Planet. Chang. 215, 103860.

Liu, J., Cao, J., Hu, G., Wang, Y., Yang, R., Liao, Z., 2020a. Water-level and redox fluctuations in a Sichuan Basin lacustrine system coincident with the Toarcian OAE. Palaeogeogr. Palaeoclimatol. Palaeoecol. 558, 109942.

Liu, M., Sun, P., Them, T.R., Li, Y., Sun, S., Gao, X., Huang, X., Tang, Y., 2020b. Organic geochemistry of a lacustrine shale across the Toarcian Oceanic Anoxic Event (Early Jurassic) from NE China. Glob. Planet. Chang. 191, 103214.

Liu, S., Yang, Y., Deng, B., Zhong, Y., Wen, L., Sun, W., Li, Z., Jansa, L., Li, J., Song, J., Zhang, X., Peng, H., 2021. Tectonic evolution of the Sichuan Basin, Southwest China. Earth-Sci. Rev. 213, 103470.

Luo, L., Qi, J., Zhang, M., 2015. Difference study on evolution and deformation of the fold-thrust belts surrounding Sichuan Basin. Geol. Rev. 61, 525–535 (in Chinese with English abstract).

Macquaker, J.H.S., Bentley, S.J., Bohacs, K.M., 2010. Wave-enhanced sediment-gravity flows and mud dispersal across continental shelves: reappraising sediment transport processes operating in ancient mudstone successions. Geology 38, 947–950.

Martini, R., Cirilli, S., Saurer, C., Abate, B., Ferruzza, G., Lo Cicero, G., 2007. Depositional environment and biofacies characterisation of the Triassic (Carnian to Rhaetian) carbonate succession of Punta Bassano (Marettimo Island, Sicily). Facies 53, 389–400.

McElwain, J.C., Wade-Murphy, J., Hesselbo, S.P., 2005. Changes in carbon dioxide during an oceanic anoxic event linked to intrusion into Gondwana Coals. Nature 435, 479–482.

Mulder, T., Syvitski, J.P.M., Migeon, S., Faugères, J.C., Savoye, B., 2003. Marine hyperpycnal flows: Initiation, behavior and related deposits. A review. Mar. Petrol. Geol. 20, 861–882.

Myrow, P.M., Tice, L., Archuleta, B., Clark, B., Taylor, J.F., Ripperdan, R.L., 2004. Flat-pebble conglomerate: its multiple origins and relationship to metre-scale depositional cycles. Sedimentology 51, 973–996.

Pálfy, J., Smith, P.L., 2000. Synchrony between early Jurassic extinction, oceanic anoxic event, and the Karoo-Ferrar flood basalt volcanism. Geology 28, 747–750.

Paredes, J.M., Giacosa, R.E., Heredia, N., 2009. Sedimentary evolution of Neogene continental deposits (ñirihuau formation) along the ñirihuau river, North Patagonian Andes of Argentina. J. S. Am. Earth Sci. 28, 74–88.

Peng, J., 2021. Sedimentology of the Upper Pennsylvanian organic-Rich Cline Shale, Midland Basin: from gravity flows to pelagic suspension fallout. Sedimentology 68, 805–833.

Pieńkowski, G., Hodbod, M., Ullmann, C.V., 2016. Fungal decomposition of terrestrial organic matter accelerated Early Jurassic climate warming. Sci. Rep. 6.

Pittet, B., Suan, G., Lenoir, F., Duarte, L.V., Mattioli, E., 2014. Carbon isotope evidence for sedimentary discontinuities in the lower Toarcian of the Lusitanian Basin (Portugal): sea level change at the onset of the Oceanic Anoxic Event. Sed. Geol. 303, 1–14.

Plint, A., 2013. Mud dispersal across a cretaceous prodelta: Storm-generated, wave-enhanced sediment gravity flows inferred from mudstone microtexture and microfacies. Sedimentology 61, 609–647.

Plink-Björklund, P., Steel, R.J., 2004. Initiation of turbidity currents: Outcrop evidence for Eocene hyperpycnal flow turbidites. Sed. Geol. 165, 29–52.

Qiu, Z., He, J., 2022. Depositional environment changes and organic matter accumulation of Pliensbachian-Toarcian lacustrine shales in the Sichuan Basin, SW China. J. Asian Earth Sci. 232, 105035.

Reading, H.G., Richards, M., 1994. Turbidite systems in deep-water basin margins classified by grain size and feeder system. AAPG Bull. 78, 792–822.

Remírez, M.N., Algeo, T.J., 2020. Carbon-cycle changes during the Toarcian (Early Jurassic) and implications for regional versus global drivers of the Toarcian oceanic anoxic event. Earth-Sci. Rev. 209, 103283.

Rivera, H.A., Le Roux, J.P., Sánchez, L.K., Mariño-Martínez, J.E., Salazar, C., Barragán, J.C., 2018. Palaeoredox conditions and sequence stratigraphy of the cretaceous storm-dominated, mixed siliciclastic-carbonate ramp in the Eastern Cordillera Basin (Colombia): evidence from sedimentary geochemical proxies and facies analysis. Sed. Geol. 372, 1–24.

Ruebsam, W., Müller, T., Kovács, J., Pálfy, J., Schwark, L., 2018. Environmental response to the early Toarcian carbon cycle and climate perturbations in the northeastern part of the West Tethys Shelf. Gondwana Res. 59, 144–158.

Ruebsam, W., Reolid, M., Sabatino, N., Masetti, D., Schwark, L., 2020. Molecular paleothermometry of the early Toarcian climate perturbation. Glob. Planet. Chang. 195, 103351.

Sami, T., Desrochers, A., 1992. Episodic sedimentation on an early Silurian, storm-dominated carbonate ramp, Becscie and Merrimack Formations, Anticosti Island, Canada. Sedimentology 39, 355–381.

Schouten, S., Van Kaam-Peters, H.M.E., Rijpstra, W.I.C., Schoell, M., Sinninghe Damste, J.S., 2000. Effects of an oceanic anoxic event on the stable carbon isotopic composition of early Toarcian carbon. Am. J. Sci. 300, 1–22.

Šegvić, B., Benvenuti, A., Moscariello, A., 2016. Illite-smectite-rich clay parageneses from Quaternary tunnel valley sediments of the dutch southern North Sea–mineral origin and paleoenvironment implications. Clay Clay Mineral. 64, 608–627.

Sell, B., Ovtcharova, M., Guex, J., Bartolini, A., Jourdan, F., Spangenberg, J.E., Vicente, J.-C., Schaltegger, U., 2014. Evaluating the temporal link between the Karoo LIP and climatic–biologic events of the Toarcian stage with high-precision U–pb geochronology. Earth Planet. Sci. Lett. 408, 48–56.

Shanmugam, G., 2008. Deep-water bottom currents and their deposits. In: Rebesco, M., Camerlenghi, A. (Eds.), Contourites. Developments in Sedimentology, 60, pp. 59–81.

Spalletti, L.A., Poiré, D.G., Schwarz, E., Veiga, G.D., 2001. Sedimentologic and sequence stratigraphic model of a neocomian marine carbonate–siliciclastic ramp: Neuquén Basin, Argentina. J. S. Am. Earth Sci. 14, 609–624.

Suan, G., Schöllhorn, I., Schlögl, J., Segit, T., Mattioli, E., Lécuyer, C., Fourel, F., 2018. Euxinic conditions and high sulfur burial near the european shelf margin (Pieniny Klippen Belt, Slovakia) during the Toarcian oceanic anoxic event. Glob. Planet. Chang. 170, 246–259.

Sumner, E.J., Amy, L.A., Talling, P.J., 2008. Deposit structure and processes of sand deposition from decelerating sediment suspensions. J. Sed. Res. 78, 529–547.

Svensen, H., Planke, S., Chevallier, L., Malthe-Sørenssen, A., Corfu, F., Jamtveit, B., 2007. Hydrothermal venting of greenhouse gases triggering early Jurassic global warming. Earth Planet. Sci. Lett. 256, 554–566.

Them, T.R., Gill, B.C., Selby, D., Gröcke, D.R., Friedman, R.M., Owens, J.D., 2017. Evidence for rapid weathering response to climatic warming during the Toarcian Oceanic Anoxic Event. Sci. Rep. 7.

Trabucho-Alexandre, J., 2014. More gaps than shale: erosion of mud and its effect on preserved geochemical and palaeobiological signals. J. Geol. Soc. Lond. 404, 251–270.

Ullmann, C.V., Thibault, N., Ruhl, M., Hesselbo, S.P., Korte, C., 2014. Effect of a Jurassic oceanic anoxic event on belemnite ecology and evolution. Proc. Natl. Acad. Sci. 111, 10073–10076.

Ullmann, C.V., Boyle, R., Duarte, L.V., Hesselbo, S.P., Kasemann, S.A., Klein, T., Lenton, T.M., Piazza, V., Aberhan, M., 2020. Warm afterglow from the Toarcian Oceanic Anoxic Event drives the success of deep-adapted brachiopods. Sci. Rep. 10.

Vörös, A., 2005. The smooth brachiopods of the Mediterranean Jurassic: Refugees or invaders? Palaeogeogr. Palaeoclimatol. Palaeoecol. 223, 222–242.

Wang, X., Jin, Z., Zhao, J., Zhu, Y., Hu, Z., Liu, G., Jiang, T., Wang, H., Li, S., Shi, S., 2020. Depositional environment and organic matter accumulation of Lower Jurassic nonmarine fine-grained deposits in the Yuanba Area, Sichuan Basin, SW China. Mar. Petrol. Geol. 116, 104352.

Wei, W., Swennen, R., 2022. Sedimentology and lithofacies of organic-rich Namurian Shale, Namur Synclinorium and Campine Basin (Belgium and S-Netherlands). Mar. Petrol. Geol. 138, 105553.

Woodfine, R.G., Jenkyns, H.C., Sarti, M., Baroncini, F., Violante, C., 2008. The response of two Tethyan carbonate platforms to the early Toarcian (Jurassic) oceanic anoxic event: environmental change and differential subsidence. Sedimentology 55, 1011–1028.

Wright, L.D., Friedrichs, C.T., Kim, S.C., Scully, M.E., 2001. Effects of ambient currents and waves on gravity-driven sediment transport on continental shelves. Mar. Geol. 175, 25–45.

Xiao, Z., Chen, S., Zhang, S., Zhang, R., Zhu, Z., Lu, J., Li, Y., Yin, X., Tang, L., Liu, Z., Lin, Z., 2021. Sedimentary environment and model for lacustrine organic matter enrichment: lacustrine shale of the Early Jurassic Da'anzhai Formation, central Sichuan Basin, China. J. Palaeogeogr. 10, 584–601.

Xu, W., Ruhl, M., Jenkyns, H.C., Hesselbo, S.P., Riding, J.B., Selby, D., Naafs, B.D.A., Weijers, J.W.H., Pancost, R.D., Tegelaar, E.W., Idiz, E.F., 2017. Carbon sequestration in an expanded lake system during the Toarcian oceanic anoxic event. Nat. Geosci. 10, 129–134.

Xu, W., Ruhl, M., Jenkyns, H.C., Leng, M.J., Huggett, J.M., Minisini, D., Ullmann, C.V., Riding, J.B., Weijers, J.W.H., Storm, M.S., Percival, L.M.E., Tosca, N.J., Idiz, E.F., Tegelaar, E.W., 2018. Evolution of the Toarcian (Early Jurassic) carbon-cycle and global climatic controls on local sedimentary processes (Cardigan Bay Basin, UK). Earth Planet. Sci. Lett. 484, 396–411.

Zavala, C., Arcuri, M., Meglio, M.D., Diaz, H.G., Contreras, C., 2011. A genetic facies tract for the analysis of sustained hyperpycnal flow deposits. In: Zavala, C., Slatt, R. (Eds.), Sediment Transfer from Shelf to Deep Water-Revisiting the Delivery System: AAPG Studies in Geology, 61, pp. 31–51.